

Efficient Bayesian-based Multi-View Deconvolution

Stephan Preibisch^{1,2,3,*}, Fernando Amat², Evangelia Stamatakis¹,
Mihail Sarov¹, Robert H. Singer^{2,3}, Gene Myers^{1,2} and Pavel Tomancak^{1,*}

¹Max Planck Institute of Molecular Cell Biology and Genetics, Pfotenhauerstrasse 108, Dresden, Germany

²HHMI Janelia Farm Research Campus, 19700 Helix Drive, Ashburn, VA 20147, USA

³Department of Anatomy and Structural Biology, Gruss Lipper Biophotonics Center, Albert Einstein College of Medicine, Bronx, NY 10461, USA

ABSTRACT

Light sheet fluorescence microscopy is able to image large specimen with high resolution by imaging the samples from multiple angles. Multi-view deconvolution can significantly improve the resolution and contrast of the images, but its application has been limited due to the large size of the datasets. Here we present a Bayesian-based derivation of multi-view deconvolution that drastically improves the convergence time and provide a fast implementation utilizing graphics hardware.

MAIN DOCUMENT

Modern light sheet microscopes¹⁻³ are able to acquire large, developing specimens with high temporal and spatial resolution typically by imaging them from multiple directions (**Fig. 1a**). The low photodamage offered by a light sheet microscopes design allows the recording of massive, time-lapse datasets that have the potential to enable the reconstruction of entire lineage trees of the developing specimen. However, accurate segmentation and tracking of nuclei and cells in these datasets remain a challenge because image quality is limited by the optical properties of the imaging system and the compromises between acquisition speed and resolution. Deconvolution utilizes knowledge about the optical system to substantially increase spatial resolution and contrast after acquisition. An advantage unique to light sheet microscopy and in particular to Selective Plane Illumination Microscopy (SPIM), is the ability to observe the same location in the specimen from multiple angles which renders the ill-posed problem of deconvolution more tractable.⁴⁻¹⁰

Richardson-Lucy (RL) deconvolution^{11,12} (**Suppl. Note Chapter 1, 2**) is a Bayesian-based derivation resulting in an iterative expectation-maximization (EM) algorithm^{5,13} that is often chosen for its simplicity and performance. Multi-view deconvolution has previously been derived using the EM framework,^{5,9,10} however the convergence time of the algorithm remains orders of magnitude longer than the time required to record the data. We address this problem by deriving an optimized formulation of Bayesian-based deconvolution for multiple view geometry that explicitly incorporates conditional probabilities between the views (**Fig. 1b,c**) and combine it with Ordered Subset Expectation Maximization (OSEM)⁶ (**Fig. 1d**) achieving significantly faster convergence (**Fig. 1d,e,f**).

Bayesian-based deconvolution models images and point spread functions (PSFs) as probability distributions. The goal is to estimate the most probable underlying distribution (deconvolved image) that explains best all observed distributions (views) given their conditional probabilities (PSFs). We first re-derived the original Richardson-Lucy deconvolution algorithm and subsequently extended it to multiple-view geometry yielding

$$f_{RL} = \int_{x_v} \frac{\phi_v(x_v)}{\int_{\xi} \psi^r(\xi) P(x_v|\xi) d\xi} P(x_v|\xi) dx_v \quad (1)$$

$$\psi^{r+1}(\xi) = \psi^r(\xi) \prod_{v \in V} f_{RL} \quad (2)$$

* Correspondence should be addressed to: preibischs@janelia.hhmi.org and tomancak@mpi-cbg.de

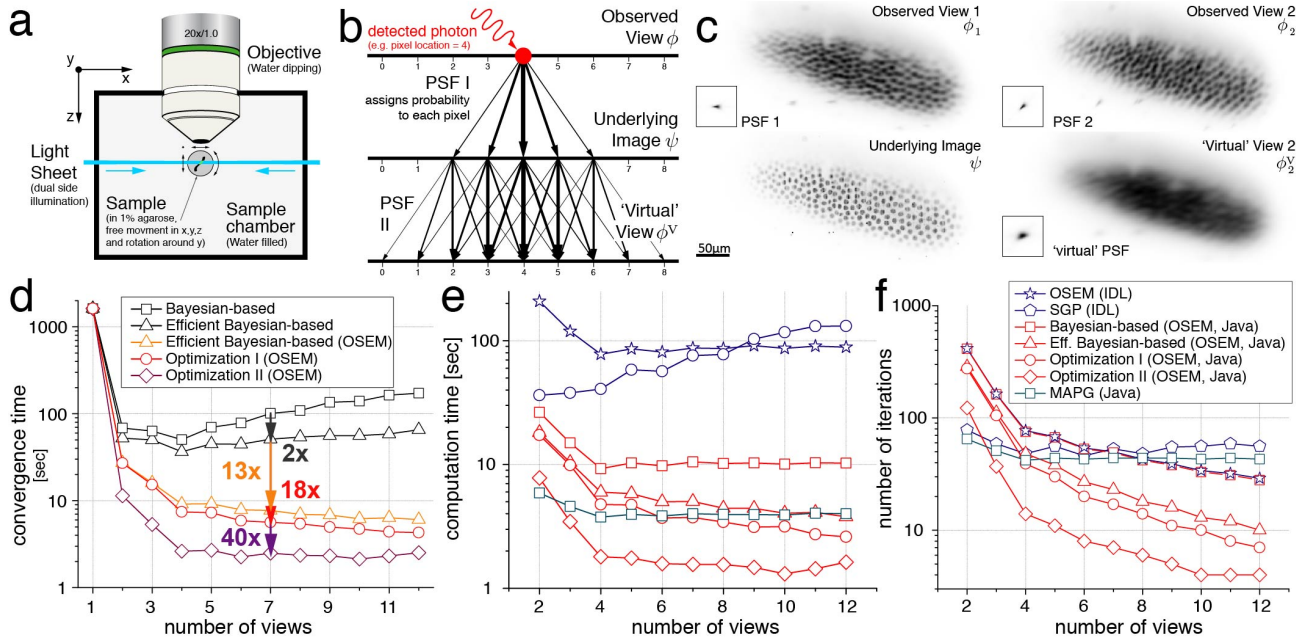


Figure 1: Principles and performance. (a) The basic layout of a light sheet microscope capable of multi-view acquisitions. (b) Illustrates the idea of virtual views. A photon detected at a certain location in a view was emitted by a fluorophore in the sample; the point-spread function assigns a probability to every location in the underlying image having emitted that photon. Consecutively, the point-spread function of any other view assigns to each of its own locations the probability to detect a photon corresponding to the same fluorophore. (c) Shows an example of an entire virtual view computed from observed view 1 and the knowledge of PSF1 and PSF 2. (d) Compares the convergence time of the different Bayesian-based methods. We used a known ground truth image (Suppl. Fig. 5) and let all variations converge until they reach precisely the same quality. Note that the increase in computation time for an increasing number of views of the combined methods (black) is due to the fact that with an increasing number of views more computational effort is required to perform one update of the deconvolved image (Suppl. Fig. 4) (e) Compares the convergence times for the same ground truth image of our Bayesian-based methods to other optimized multi-view deconvolution algorithms.⁵⁻⁸ Note that part of the huge difference to OSEM and SGP is the result of not optimized IDL code. (f) Compares the corresponding number of iterations in comparison to other optimized multi-view deconvolution algorithms. Note that the Java and IDL implementation of OSEM perform almost identically.

where $\psi(\xi)$ denotes the deconvolved image at iteration r , $\phi_v(x_v)$ the input views, both as functions of their respective pixel locations ξ and x_v , while $P(x_v|\xi)$ denotes the individual PSFs (Suppl. Note Chapter 2, 3). Equation 1 denotes a classical RL update step for one view; equation 2 illustrates the combination of all views into one update of the deconvolved image. Our equation suggests a multiplicative combination, in contrast to maximum-likelihood expectation-maximization⁵ that combines RL updates by addition. We prove that equation 2 also converges to the Maximum-Likelihood (ML) solution (Suppl. Note Chapter 4), while it is important to note that the ML solution is not necessarily the correct solution if disturbances like noise or misalignments are present in the input images. Importantly, previous extensions to multiple views⁵⁻¹⁰ are based on the assumption that the individual views are independent observations (Suppl. Fig. 2). Assuming independence between two views implies that by observing one view, nothing can be learned about the other view. We show that this independence assumption is not required to derive equation 2. Thus our solution represents the first complete derivation of Richardson-Lucy multi-view deconvolution based on probability theory and Bayes theorem.

As we do not need to consider views to be independent, we next asked if the conditional probabilities describing the relationship between two views can be modeled and used in order to improve convergence behavior (Suppl. Note Chapter 7). Assuming that a single photon is observed in the first view, the PSF of this view and Bayes theorem can be used to assign a probability to every location in the deconvolved image having

emitted this photon (**Fig. 1b**). Based on this probability distribution, the PSF of the second view directly yields the probability distribution describing where to expect a corresponding observation for the same fluorophore in the second view (**Fig. 1b**). Following this reasoning, we argue that it is possible to compute an approximate image (virtual view) of one view from another view provided that the PSFs of both views are known (**Fig. 1c**).

We use these virtual views to perform intermediate update steps at no additional computational cost, decreasing the computational effort approximately 2-fold (**Fig. 1d**) and **Suppl. Note Chapter 7**). The multiplicative combination (equation 2) directly suggests a sequential approach, where each RL update (equation 1) is directly applied to $\psi(\xi)$ (**Suppl. Fig. 2**). This sequential scheme is equivalent to the OSEM⁶ algorithm and results in a 13-fold decrease in convergence time. This gain increases linearly with the number of views⁶ (**Fig. 1d** and **Suppl. Fig. 4**). The new algorithm also performs well in the presence of noise and imperfect point spread functions (**Suppl. Fig. 7,8,9**). To further reduce convergence time we introduce ad-hoc simplifications (optimization I & II) for the estimation of conditional probabilities that achieve up to 40-fold improvement compared to deconvolution methods that assume view independence (**Fig. 1d,e,f**, **Suppl. Fig. 4** and **Suppl. Note Chapter 10**). If the input views show very low signal-to-noise ratio (atypical for SPIM) the speed-up is preserved but the quality of the deconvolved image is reduced. Our Bayesian-based derivation does not assume a specific noise model but it is in practice robust to Poisson noise, which is the dominating source of noise in light-sheet microscopy acquisitions (**Suppl. Fig. 6,7**). As a compromise between quality and speed we use, if not stated otherwise, the intermediate optimization I for all deconvolution experiments on real datasets.

We compared the performance of our method with previously published multi-view deconvolution algorithms⁵⁻¹⁰ in terms of convergence behavior and runtime on the CPU (**Fig. 1e,f**, **Fig. 2d** and **Suppl. Fig. 4b, 6a,b**). For typical SPIM multi-view scenarios consisting of around 7 views with a high signal-to-noise ratio our method requires 7 fold fewer iterations compared to OSEM,⁶ Scaled Gradient Projection (SGP)⁸ and Maximum a posteriori with Gaussian Noise (MAPG)⁷ while being 50 fold faster than the IDL implementation of SGP, 7 fold faster than OSEM and 3 fold faster than MAPG (implemented in Java). At the same time our optimization is able to improve the visual image quality of real and simulated datasets compared to MAPG (**Fig. 2e,f** and **Suppl. Fig. 6c-h**). Further speed up of 3 fold and reduced memory consumption is achieved by using CUDA implementation (**Suppl. Fig. 17e**). On real datasets that are often characterized by partial overlap of the input data, the actual overall computation time is increased due to missing data and the overheads imposed by boundary conditions (**Suppl. Fig. 17** and **Suppl. Note Chapter 12**). However, our approach is capable of dealing with partially overlapping acquisitions.

In order to evaluate the quality and performance of our algorithm on realistic three-dimensional multi-view image data we generated a simulated ground truth dataset resembling a biological specimen (**Fig. 2a**). We next simulated how this dataset looks like when imaged in a SPIM microscope from multiple angles by applying signal attenuation across the field of view, convolving the data with the PSF of the microscope, simulating the multi-view optical sectioning and using a Poisson process to generate the final pixel intensities (**Fig. 2b** and **Suppl. Note Chapter 13**). We deconvolved the generated multi-view data (**Fig. 2c**) using our algorithm with and without regularization and compared the result to the content based fusion and the MAPG deconvolution (**Fig. 2d-f**). The results show that our algorithm reaches optimal reconstruction quality faster (**Fig. 2d**), introduces less artifacts compared to MAPG (**Fig. 2e,f**, note the artificial ring artifacts, and Supplementary video 2 and 3, note the artificial patterns in yz for MAPG) and that regularization is required to achieve convergence under realistic imaging conditions that we simulated (**Fig. 2d,f**).

Prerequisite for multi-view deconvolution of light sheet microscopy data are precisely aligned multi-view datasets and estimates of point spread functions for all views. We exploit the fact that for the purposes of registration we include sub-resolution fluorescent beads into the rigid agarose medium in which the specimen is embedded. The beads are initially used for multi-view registration of the SPIM data¹⁴ and subsequently to extract the PSF for each view for the purposes of multi-view deconvolution. We average the intensity of PSFs for each view for all the beads that were identified as corresponding during registration yielding a precise measure of the PSF for each view under the specific experimental condition. This synergy of registration and

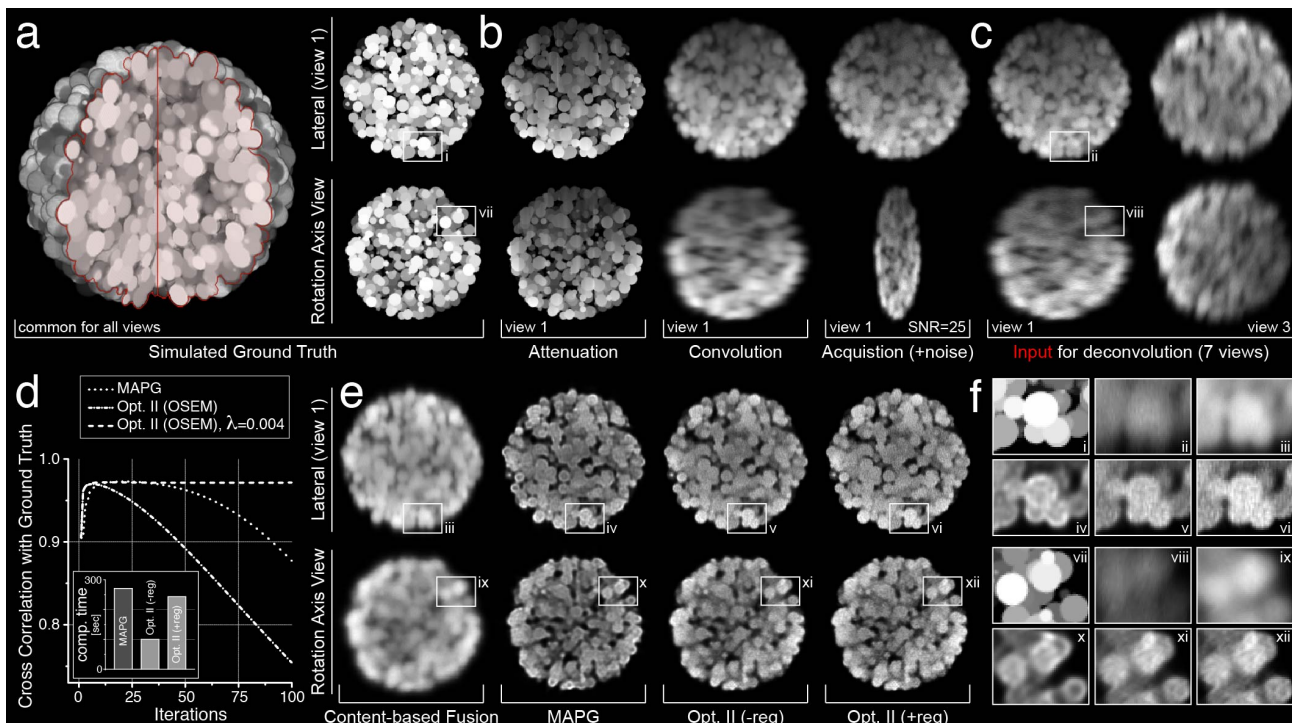


Figure 2: Deconvolution of simulated three dimensional multi-view data. **(a)** On the left 3d rendering of a computer generated volume resembling a biological specimen. Red line marks the wedge removed from the volume to show the content inside. On the right sections through the generated volume in lateral direction (as seen by the SPIM camera, top) and along the rotation axis (bottom). **(b)** The same slice as in **(a)** with illumination attenuation applied (left), convolved with PSF of a SPIM microscope (middle) and image simulated using a poisson process (right). The bottom right panel shows the unscaled simulated light sheet sectioning data along the rotation axis. **(c)** Slices from view one and three of the seven views generated from **(a)** by applying processes pictured in **(b)** and rescaling to isotropic resolution. These seven volumes are the input to the fusion and deconvolution algorithms quantified in **(d)** and visualized in **(e)**. **(d)** plots the cross-correlation of deconvolved and ground truth data as a function of the number of iterations for MAPG and our algorithm with and without regularization. The inset compares the computational time (both algorithms were implemented in Java to support partially overlapping datasets, **Suppl. Fig. 17**). **(e)** slices equivalent to **(c)** after content based fusion (first column), MAPG deconvolution (second column), our approach without regularization (third column) and with regularization (fourth column, $\lambda=0.004$). **(f)** shows areas marked by boxes in **(b,c,e)** at higher magnification.

deconvolution ensures realistic representation of PSFs under any imaging condition. Alternatively, simulated PSFs or PSFs measured by other means can be provided as inputs to the deconvolution algorithm.

We applied our deconvolution approach to multi-view SPIM acquisitions of *Drosophila* and *C. elegans* embryos (**Fig. 3a-e**). We achieve a significant increase in contrast as well as resolution with respect to the content-based fusion¹⁴ (**Fig. 3b** and **Suppl. Fig. 14**), while only a few iterations are required and computation times are typically in the range of a few minutes per multi-view acquisition (**Suppl. Table 1**). A remaining challenge for creating a complete computational model of *C. elegans* larvae in L1 stage is to be able to identify all nuclei in the nervous system.¹⁵ We applied the deconvolution to a 4-view acquisition of a fixed specimen expressing GFP tagged lamin (LMN-1::GFP) labeling the nuclear lamina and stained for DNA with Hoechst (**Fig. 3f,g**). Running the multi-view deconvolution for 100 iterations using optimization II, we achieve a significantly improved contrast and resolution compared the input data acquired with the Zeiss Lightsheet Z.1 microscope. Previous attempts to segment nuclei in confocal images of L1 worm resulted in unambiguous identification of 357 of the 558 nuclei.¹⁵ Our deconvolved dataset allows the manual segmentation of all 558 nuclei with uncertainty of about 5 nuclei among annotation trials.

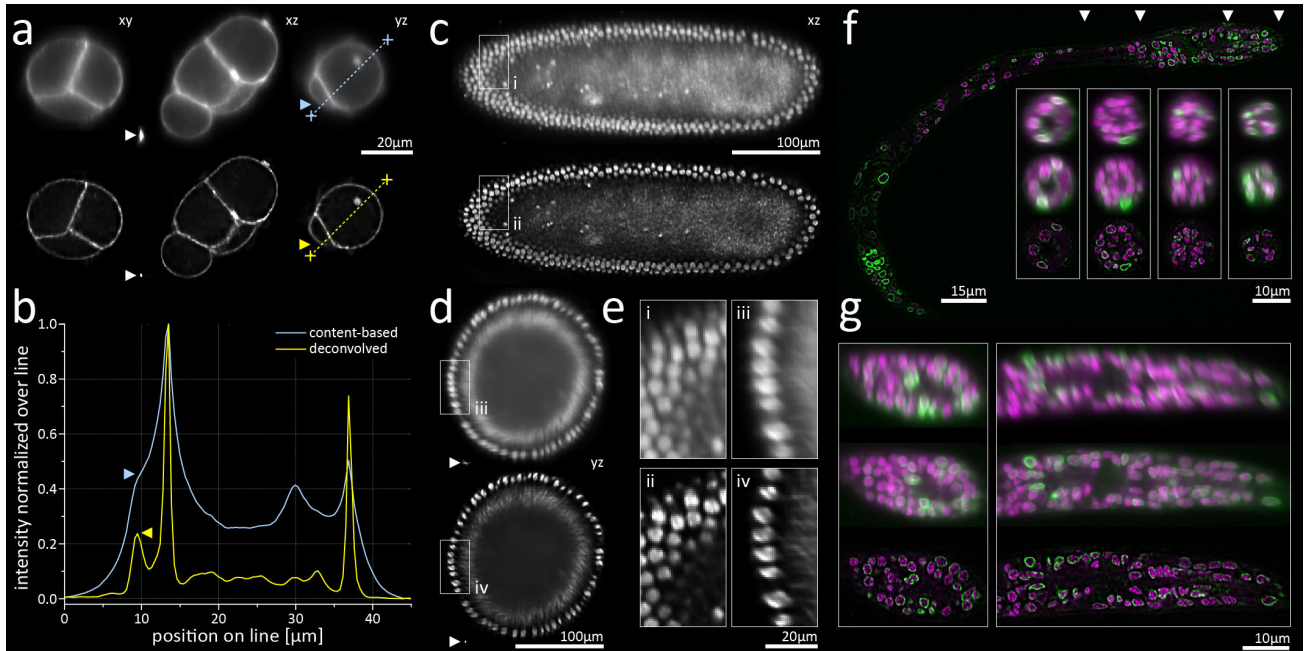


Figure 3: Application to biological data. (a) Comparison of reconstruction results using content-based fusion (upper row) and multi-view deconvolution (lower row) on a 4-cell stage *C. elegans* embryo expressing PH-domain-GFP fusion marking the membranes. Dotted lines mark plots shown in (b), white arrows mark PSFs of a fluorescent bead before and after deconvolution. (b) Line plot through the volume along the rotation axis (yz), typically showing lowest resolution in light sheet acquisitions. Contrast along the line is locally normalized. Signal-to-noise is significantly enhanced, arrows mark points that illustrate increased resolution. (c,d) show cut planes through a blastoderm stage *Drosophila* embryo expressing His-YFP in all cells. White boxes mark areas magnified in (e). Detailed comparison of computation times for this dataset is shown in Fig. 1e. (e) Magnified view on small parts of the *Drosophila* embryo. Left panel shows one of the directly acquired views, right panel shows a view along the rotation axis usually characterized by the lowest resolution. (f,g) Comparison of the deconvolved image data to the input data of a fixed *C. elegans* larvae in L1 stage expressing LMN-1-GFP (green) and stained with Hoechst (magenta). (f) Single slice through the deconvolved dataset, arrows mark 4 locations of transversal cuts shown below. The cuts compare two orthogonal input views (0, 90 degrees) with the deconvolved data. Note that no input view offers high resolution in this orientation approximately along the rotation axis. (g) The first row of the left box shows a random slice of a view in axial orientation marking the worst possible resolution of the microscope. The second row shows an input view in lateral orientation, i.e. the best possible resolution achieved by the microscope. The third row shows the corresponding deconvolved image. The box on the right shows a random slice through the nervous system. Note that the alignment of the *C. elegans* L1 dataset was refined using nuclear positions as described in **Suppl. Note Chapter 15**.

The results of multi-view deconvolution on SPIM data are equivalent to the application of Structured Illumination in SPIM¹⁶ providing a convenient post-processing alternative to increasing contrast (**Suppl. Fig. 11**). Moreover, we show that multi-view deconvolution produces superior results when comparing an acquisition of the same sample with SPIM and two-photon microscope (**Suppl. Fig. 12**). Finally, the benefits of the multi-view deconvolution approach are not limited to SPIM as illustrated by the deconvolved multi-view Spinning Disc Confocal Microscope acquisition of *C. elegans* L1 larva¹⁴ (**Suppl. Fig. 13**). Taken together these results illustrate that our multi-view deconvolution can be applied to increase the resolution of optical sectioning microscopy universally.

The increased contrast and resolution are especially visible on samples acquired with thicker light sheets such as in the case of OpenSPIM¹⁷ (**Suppl. Fig. 15**). Out-of-focus light is significantly reduced and individual nuclei become separable even in orientations perpendicular to the rotation axis that have not been imaged by the microscope directly. Also very large datasets, such as the acquisition of *Drosophila* ovaries, with input data of over 5 billion voxels become computable in reasonable time (**Suppl. Fig. 16** and **Suppl. Table 1**). To

further substantiate the utility of the algorithm we deconvolved an entire time-course of *Drosophila* embryonic development consisting of 236 time-points). The computation time was 24 hours using two Nvidia Quadro 4000 graphics cards, highlighting the performance and applicability of the method to very large datasets.

A major obstacle for widespread application of deconvolution approaches to multi-view light sheet microscopy data is lack of usable and scalable multi-view deconvolution software. We integrated our fast converging algorithm into Fiji's¹⁸ multi-view processing pipeline as open-source plugin where it complements existing approaches to multi-view data registration (http://fiji.sc/Multi-View_Deconvolution). We provide an efficient implementation for GPU and CPU taking advantage of ImgLib.¹⁹ It offers processing times of a few minutes (**Suppl. Table 1**), comparable to the acquisition rates of common light sheet microscopes such as OpenSPIM or Lightsheet Z.1 (Carl Zeiss Microimaging). The long-term time-lapse acquisitions derived from Lightsheet Z.1 are truly massive (2.16 TB for 6 view 715 timepoint *Drosophila* embryogenesis recording) but our deconvolution plugin can process them in parallel on a computer cluster in real time, i.e. the same time it takes to acquire the data. To account for potential noise in the input images we added an option for Tikhonov regularization²⁰ (**Suppl. Fig. 7,8**). The deconvolution can be processed on the entire image at once for optimal performance or in blocks to reduce the memory requirements. The only free parameter of the method that must be chosen by the user is the number of iterations for the deconvolution process (**Suppl. Fig. 4,5**). We facilitate this choice by providing a debug mode allowing the user to inspect all intermediate iterations and identify optimal tradeoff between quality and computation time. For a typical multi-view acquisition comprising 68 views we suggest between 10-15 iterations.

One of the challenges in image deconvolution is to arrive at the correct solution quickly without compromising quality. We have achieved significant improvement in convergence time over existing methods by exploiting conditional probabilities between views in a multi-view deconvolution scenario, while producing visually identical or improved results at SNRs typical for light-sheet microscopy (**Fig. 2e,f** and **Suppl. Fig. 6c-h**). We have further implemented the algorithm as an open source GPU accelerated software in Fiji where it synergizes with other related plugins into an integrated solution for the processing of multi-view light sheet microscopy data of arbitrary size.

ACKNOWLEDGMENTS

We thank Tobias Pietzsch for very helpful discussions, proofreading and access to his unpublished software, Nathan Clack, Fernando Carrillo Oesterreich and Hugo Bowne-Anderson for discussions, Nicola Maghelli for two-photon imaging, Peter Verveer for his source code and helpful discussions, Michael Weber for imaging the *Drosophila* time series, Steffen Jaensch for preparing the *C. elegans* embryo, Jun Kelly Liu for the LW698 strain, Stephan Saalfeld for help with 3D rendering, P.J. Keller for supporting F.A. and the SI-SPIM dataset, Albert Cardona for access to his computer and Carl Zeiss Microimaging for providing us with the SPIM prototype. S.P. was supported by MPI-CBG, HHMI and the Human Frontier Science Program (HFSP) Postdoctoral Fellowship in R.H.S. lab, with additional support from NIH GM57071. F.A. was supported by HHMI. G.M. was supported by HHMI and MPI-CBG. P.T. was supported by The European Research Council Community's Seventh Framework Program (FP7/2007-2013) grant agreement 260746.

AUTHOR CONTRIBUTIONS

S.P. and F.A. derived the equations for multi-view deconvolution. S.P. implemented the software and performed all analysis, F.A. implemented the GPU code. E.S. generated and imaged H2Av-mRFP *Drosophila* fly line. M.S. prepared and M.S. and S.P. imaged the *C. elegans* L1 sample. S.P. & P.T. conceived the idea and wrote the manuscript. R.H.S. provided support and encouragement, G.M. & P.T. supervised the project.

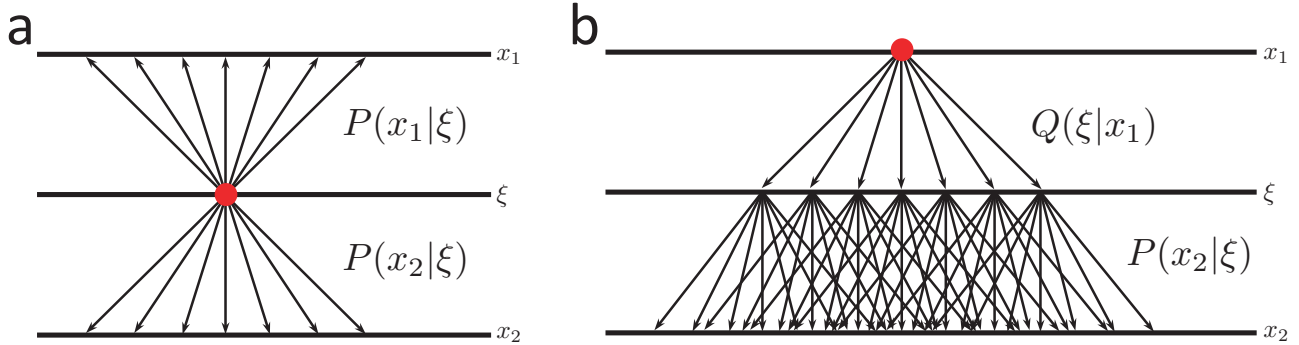
SUPPLEMENTARY MATERIAL

Supplementary File	Title
Supplementary Figure 1	Illustration of conditional probabilities describing the dependencies of two views
Supplementary Figure 2	The principle of 'virtual' views and sequential updating
Supplementary Figure 3	Illustration of assumption required for incorporating 'virtual' views without additional computational effort
Supplementary Figure 4	Performance comparison of the multi-view deconvolution methods and dependence on the PSF
Supplementary Figure 5	Images used for analysis and visual performance
Supplementary Figure 6	Comparison to other optimized multi-view deconvolutions
Supplementary Figure 7	Effect of noise on the deconvolution results
Supplementary Figure 8	Intermediate stages of deconvolution results for varying SNR's and regularization
Supplementary Figure 9	Quality of deconvolution for imprecise estimation of the PSF
Supplementary Figure 10	Variation of PSF across the light sheet in SPIM acquisitions
Supplementary Figure 11	Comparison of Multi-View Deconvolution to Structured Illumination Light Sheet Data
Supplementary Figure 12	Comparison of Multi-View Deconvolution to two-photon microscopy
Supplementary Figure 13	Multi-View Deconvolution of Spinning-Disc Confocal Data
Supplementary Figure 14	Quantification of resolution enhancement by Multi-View Deconvolution
Supplementary Figure 15	Reconstruction quality of an OpenSPIM acquisition
Supplementary Figure 16	Quality of reconstruction of Drosophila ovaries
Supplementary Figure 17	Effects of partial overlap and CUDA performance
Supplementary Table 1	Summary of datasets used in this publication
Supplementary Note	Detailed derivations and discussion of the efficient Bayesian-based multi-view deconvolution

Overview of supplementary material.

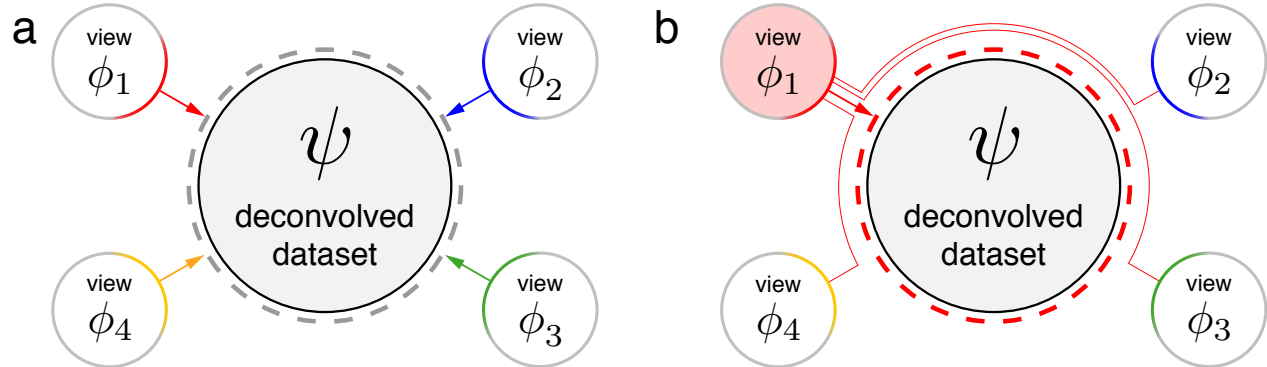
SUPPLEMENTARY FIGURES

SUPPLEMENTARY FIGURE 1 — Illustration of conditional probabilities describing the dependencies of two views



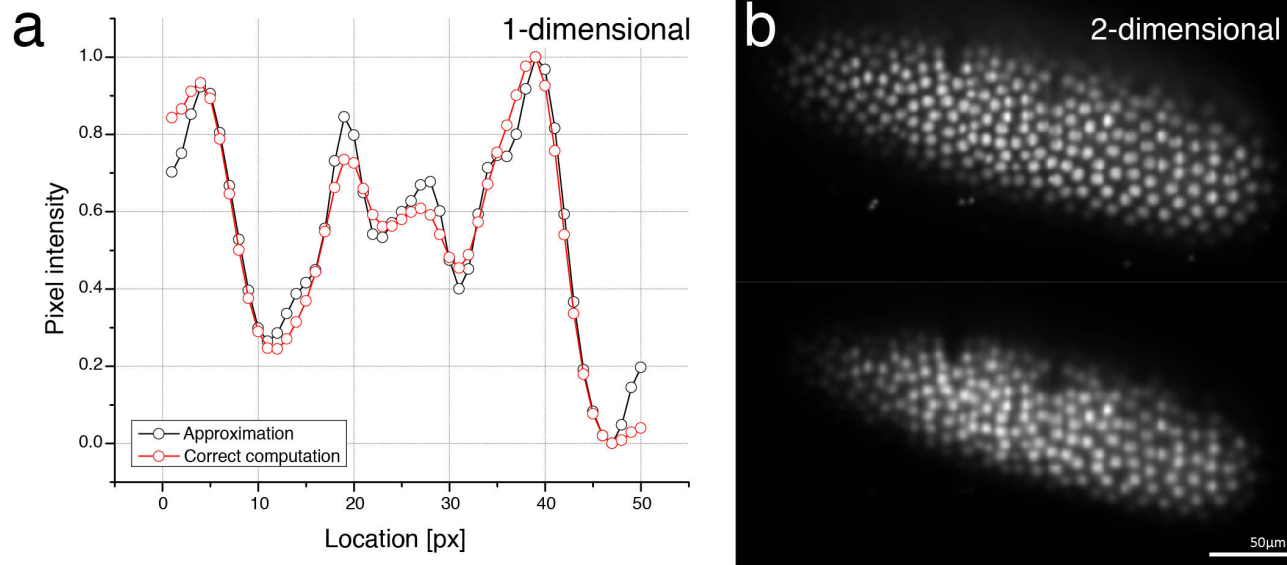
Supplementary Figure 1: Illustration of conditional probabilities describing the dependencies of two views. **(a)** illustrates the conditional independence of two observed distributions $\phi_1(x_1)$ and $\phi_2(x_2)$ if it is known that the event $\xi = \xi'$ on the underlying distribution $\psi(\xi)$ occurred. Given $\xi = \xi'$, both distributions are conditionally independent, the probability where to expect an observation only depends on $\xi = \xi'$ and the respective individual point spread function $P(x_1|\xi)$ and $P(x_2|\xi)$, i.e. $P(x_1|\xi, x_2) = P(x_1|\xi)$ and $P(x_2|\xi, x_1) = P(x_2|\xi)$. **(b)** illustrates the relationship between an observed distribution $\phi_2(x_2)$ and $\phi_1(x_1)$ if the event $x_1 = x'_1$ occurred. Solely the 'inverse' point spread function $Q(\xi|x_1)$ defines the probability for any event $\xi = \xi'$ to have caused the observation $x_1 = x'_1$. The point spread function $P(x_2|\xi)$ consecutively defines the probability where to expect a corresponding observation $x_2 = x'_2$ given the probability distribution $\psi(\xi)$.

SUPPLEMENTARY FIGURE 2 — The principle of 'virtual' views and sequential updating



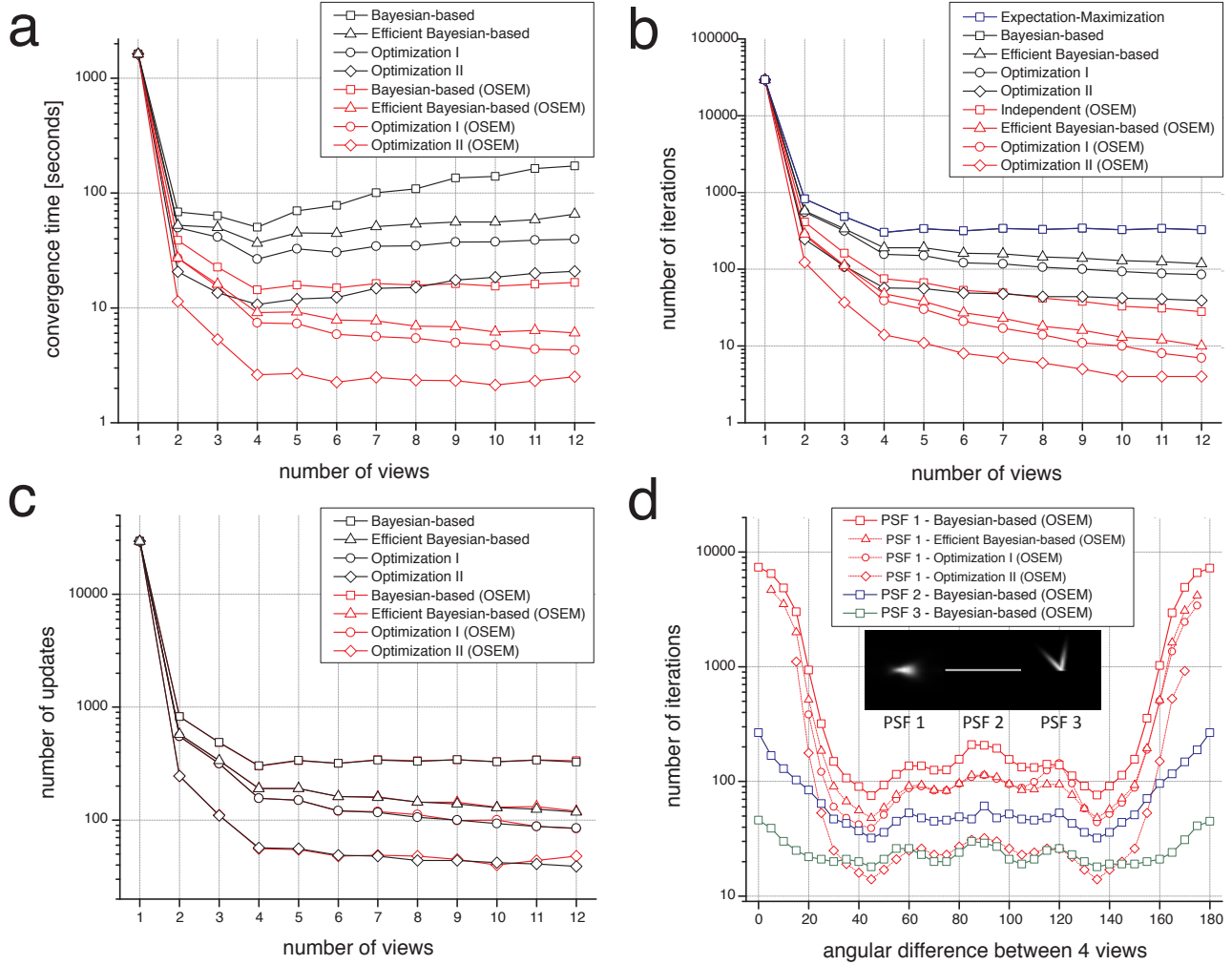
Supplementary Figure 2: The principle of 'virtual' views and sequential updating. **(a)** The classical multi-view deconvolution^{5,8-10} where an update step is computed individually for each view and subsequently combined into one update of the deconvolved image. **(b)** Our new derivation considering conditional probabilities between views. Each individual update step takes into account all other views using virtual views and additionally updates the deconvolved image individually, i.e. updates are performed sequentially⁶ and not combined.

SUPPLEMENTARY FIGURE 3 — Illustration of assumption required for incorporating 'virtual' views without additional computational effort



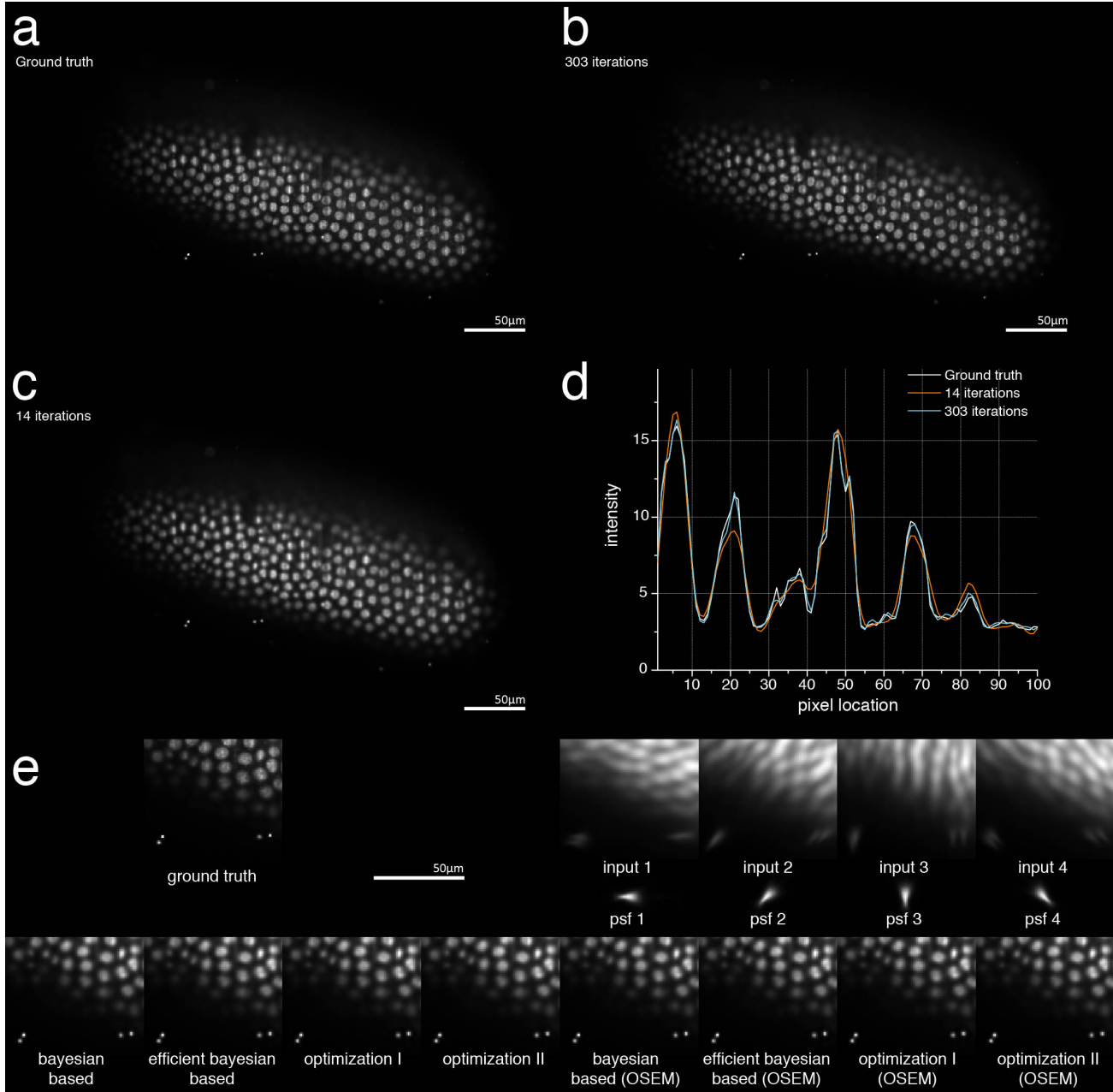
Supplementary Figure 3: Illustration of assumption in equation 93. (a) shows the difference in the result when computing $(f * g) \cdot (f * h)$ in red and the approximation $f * (g \cdot h)$ in black for a random one-dimensional input sequence (f) and two kernels with $\sigma=3$ (g) and $\sigma=2$ (h) after normalization. (b) shows the difference when using the two-dimensional image from supplementary figure 5a as input (f) and the first two point spread functions from supplementary figure 5e as kernels (g, h). The upper panel pictures the approximation, the lower panel the correct computation. Note that for (a,b) the approximation is slightly less blurred. Note that the beads are also visible in the lower panel when adjusting the brightness/contrast.

SUPPLEMENTARY FIGURE 4 — Performance comparison of the multi-view deconvolution methods and dependence on the PSF



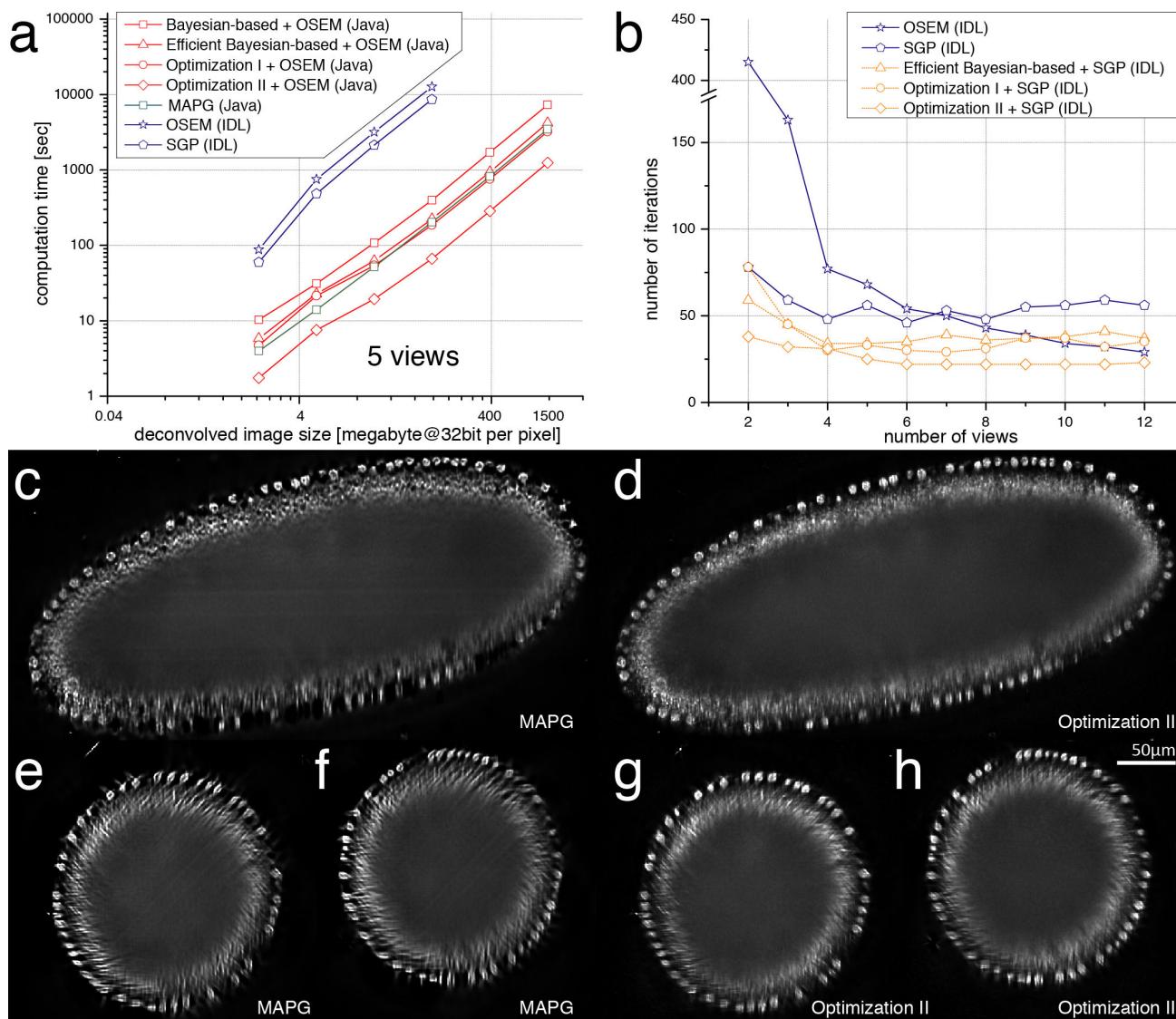
Supplementary Figure 4: Performance comparison and dependence on the PSF (a) The convergence time of the different algorithms until they reach the same average difference to the ground truth image shown in supplementary figure 5e. (b) The number of iterations required until all algorithms reach the same average difference to the ground truth image. One 'iteration' comprises all computational steps until each view contributed once to update the underlying distribution. Note that our Bayesian-based derivation and the Maximization-Likelihood Expectation-Maximization⁵ method perform almost identical (c) The total number of updates of the underlying distribution until the same average difference is reached. (d) The number of iterations required until the same difference to the ground truth is achieved using 4 views. The number of iterations is plotted relative to the angular difference between the input PSFs. An angular difference of 0 degrees refers to 4 identical PSFs and therefore 4 identical input images, an example of an angular difference of 45 degrees is shown in supplementary figure 5e. Plots are shown for different types of PSFs. (a-d) y-axis has logarithmic scale, all computations were performed on a dual-core Intel Core i7 with 2.7Ghz.

SUPPLEMENTARY FIGURE 5 — Images used for analysis and visual performance



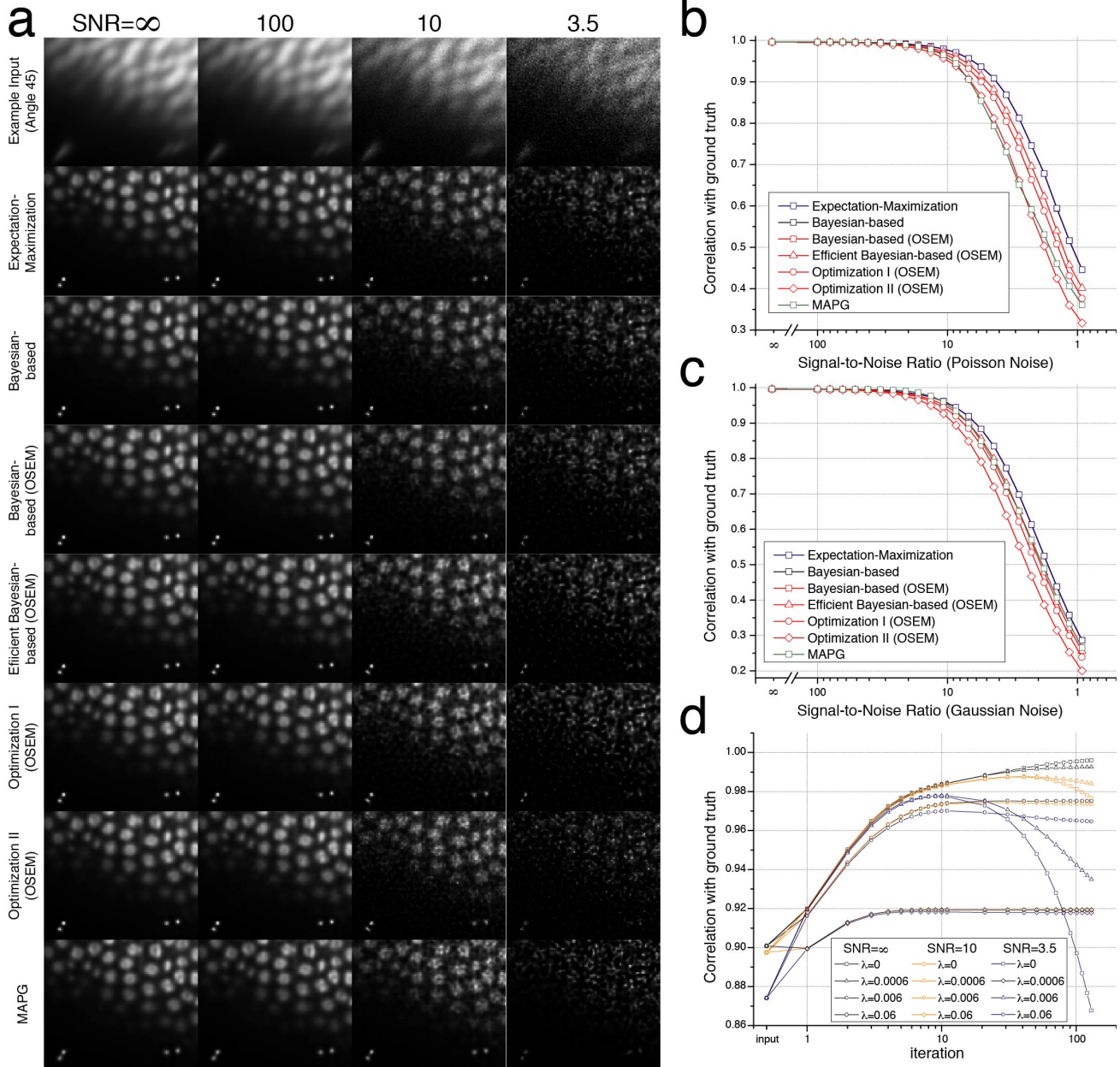
Supplementary Figure 5: Images used for analysis and visual performance. (a) The entire ground truth image used for all analyses shown in the supplement. (b) Reconstruction quality after 301 iterations using optimization II and sequential updates on 4 input views and PSF's as shown in (e). (c) Reconstruction quality after 14 iterations for the same input as (b). (d) Line-plot through the image highlighting the deconvolution quality after 301 (b) and 14 (c) iterations compared to the ground truth (a). (e) Magnification of a small region of the ground truth image (a), the 4 input PSF's and 4 input datasets as well as the results for all algorithms as used in supplementary figure 4a-c for performance measurements.

SUPPLEMENTARY FIGURE 6 — Comparison to other optimized multi-view deconvolutions



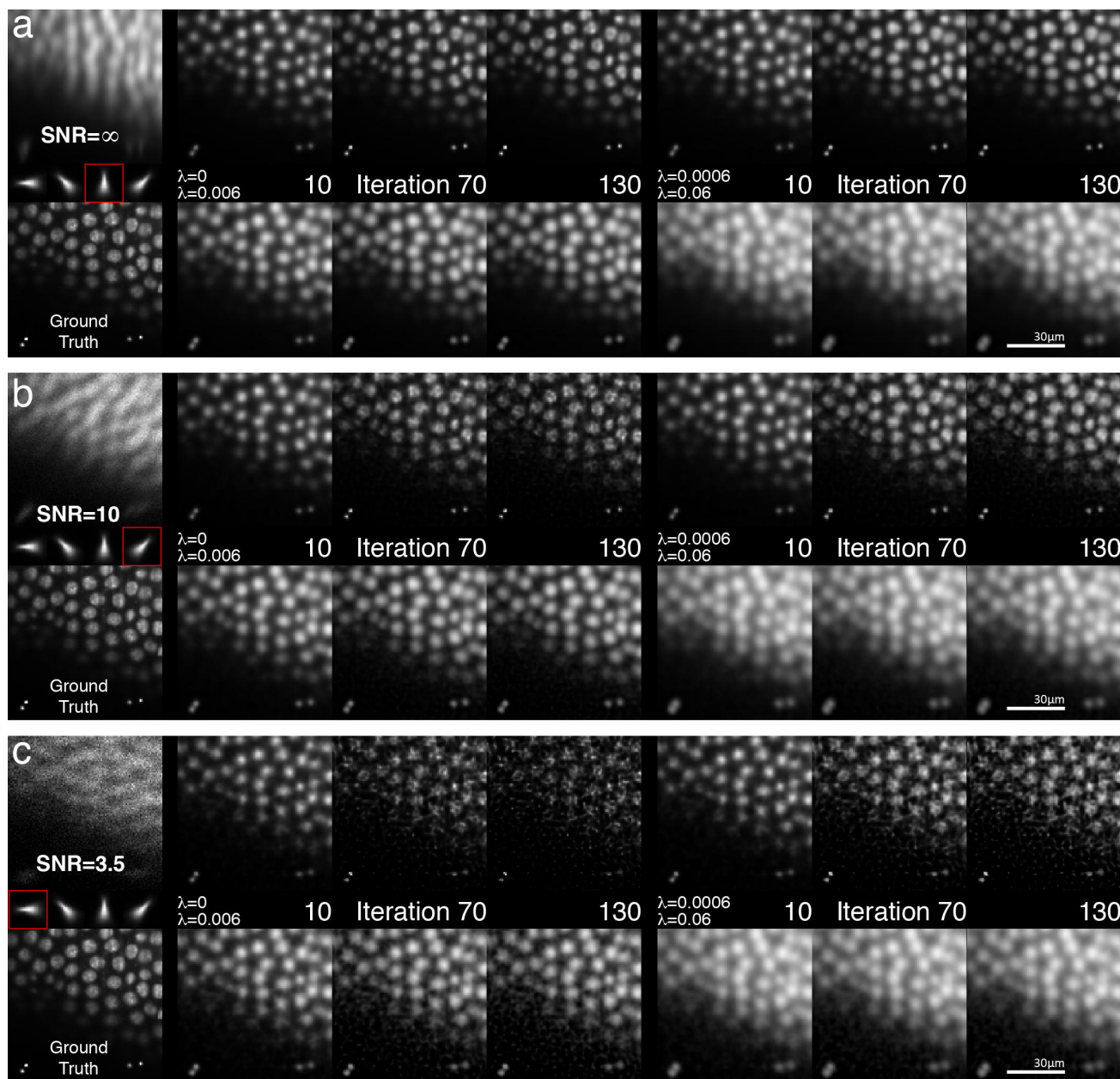
Supplementary Figure 6: Comparison to other optimized multi-view deconvolution schemes. **(a,b)** Compares optimized versions of multi-view deconvolution, including the IDL implementations of Scaled Gradient Projection (SGP),⁸ Ordered Subset Expectation Maximization (OSEM),⁶ Maximum a posteriori with Gaussian Noise (MAPG),⁷ and our derivations combined with OSEM (see also main text figure 1e,f). All computations were performed on a machine with 128 GB of RAM and two 2.7 GHz Intel E5-2680 processors. **(a)** Correlates computation time and image size until the deconvolved image reached the same difference to the known ground truth image. All algorithms perform relatively proportional, however the IDL implementations run out of memory. **(b)** illustrates that our optimizations can also be combined with SGP in order to achieve a faster convergence. **(c-h)** compare the reconstruction quality of MAPG and Optimization II using the 7-view acquisition of the *Drosophila* embryo expressing His-YFP (main text figure 3c,d,e). Without ground truth we chose a stage of similar sharpness (26 iterations of MAPG and 9 iterations of Optimization II, approximately in correspondence with main figure 1f) not using any regularization. Optimization II achieves a visually higher image quality, while MAPG shows some artifacts and enhances the stripe pattern arising from partially overlapping input images. **(c,d)** show a slice in lateral orientation of one of the input views, **(e-h)** show slices perpendicular to the rotation axis.

SUPPLEMENTARY FIGURE 7 — Effect of noise on the deconvolution results



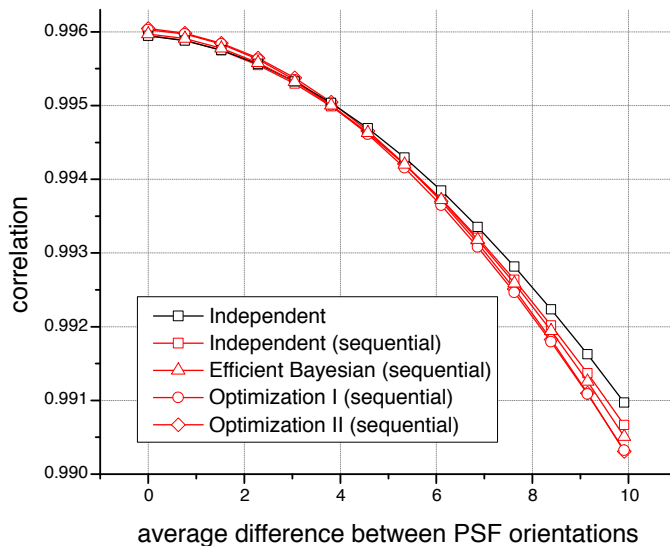
Supplementary Figure 7: Effect of noise on the deconvolution results. (a) Deconvolved images corresponding to the points in graph (b) to illustrate the resulting image quality corresponding to a certain correlation coefficient. (b,c) The resulting cross-correlation between the ground truth image and the deconvolved image depending on the signal-to-noise ratio in the input images. (b) Poisson noise, (c) Gaussian noise. (d) The cross correlation between the ground truth image and the deconvolved image at certain iteration steps during the deconvolution shown for different signal-to-noise ratios (SNR= ∞ [no noise], SNR=10, SNR=3.5) and varying parameters of the Tikhonov regularization ($\lambda=0$ [no regularization], $\lambda=0.0006$, $\lambda=0.006$, $\lambda=0.06$). Supplementary figure 8 shows the corresponding images for all data points in this plot. This graph is based on the Bayesian-based derivation using sequential updates in order to be able to illustrate the behaviour in early stages of the deconvolution.

SUPPLEMENTARY FIGURE 8 — Intermediate stages of deconvolution results for varying SNR's and regularization



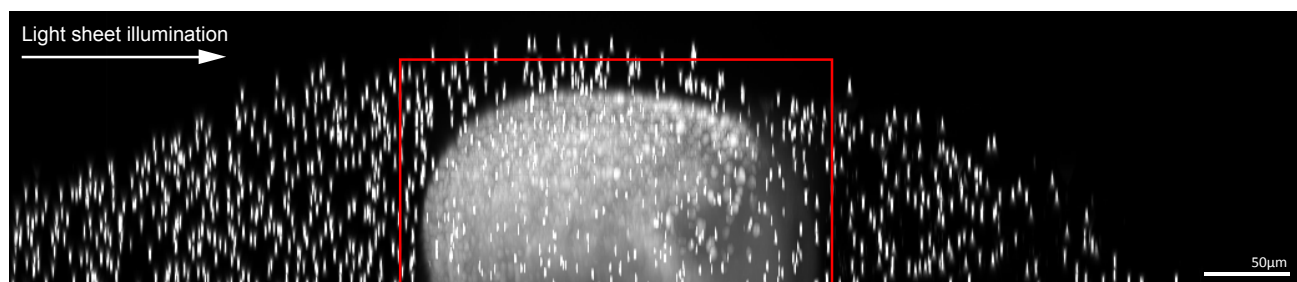
Supplementary Figure 8: Intermediate stages of deconvolution results for varying SNR's and regularization. (a-c) 1st row shows input data for the PSF in the red box, PSF's and ground truth, the other rows show the images at iteration 10, 70 and 130 for varying parameters of the Tikhonov regularization ($\lambda=0$ [no regularization], $\lambda=0.0006$, $\lambda=0.006$, $\lambda=0.06$). (a) Results and input for SNR=∞ (no noise). Here, $\lambda=0$ shows best results. (b) Results and input for SNR=10 (Poisson noise). Small structures like the fluorescent beads close to each other remain separable. (c) Results and input for SNR=3.5 (Poisson noise). Note that although the beads cannot be resolved anymore in the input data, the deconvolution produces a reasonable result, visually best for a λ between 0.0006 and 0.006.

SUPPLEMENTARY FIGURE 9 — Quality of deconvolution for imprecise estimation of the PSF



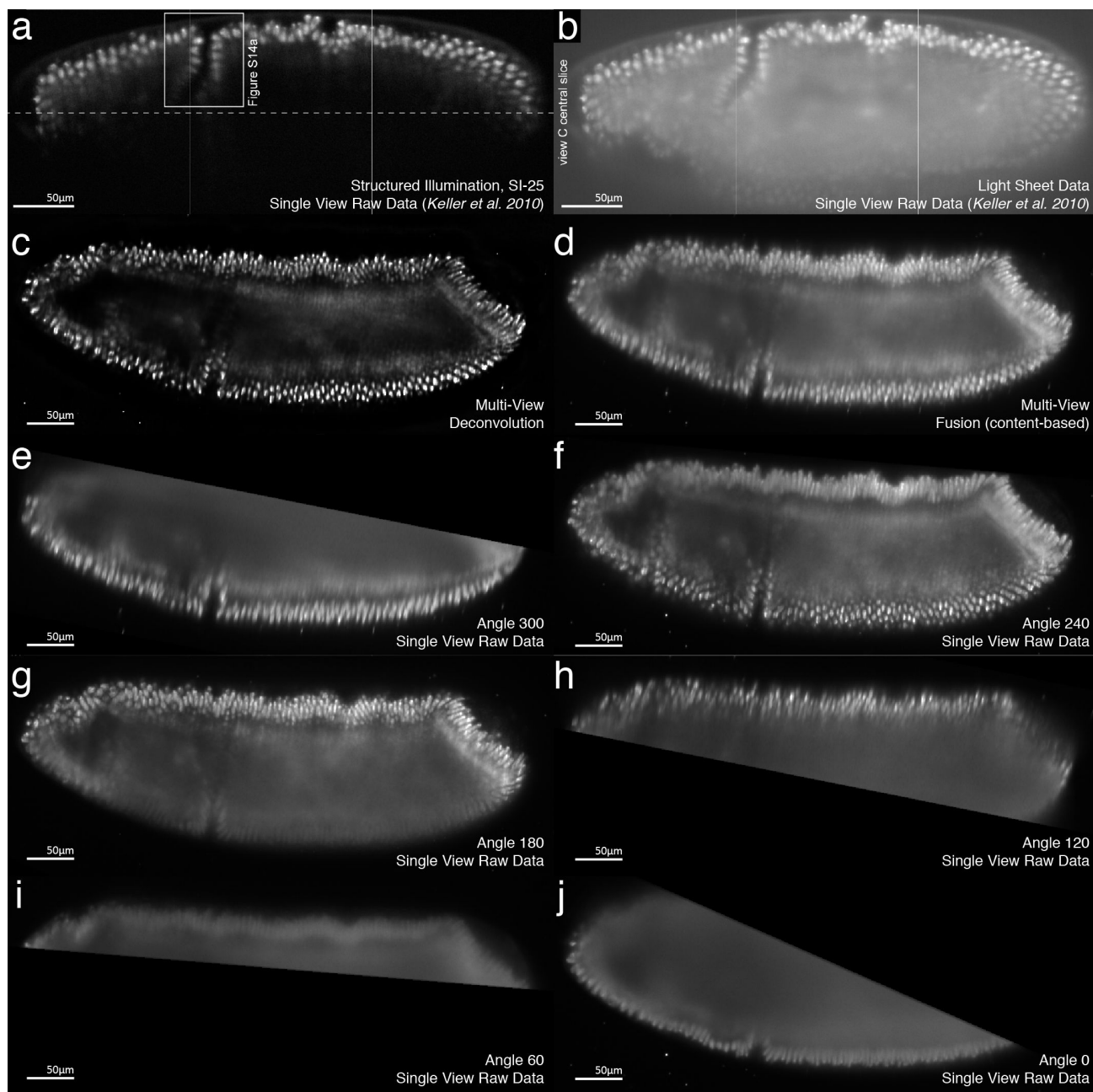
Supplementary Figure 9: Quality of deconvolution for imprecise estimation of the PSF. The cross-correlation between the deconvolved image and the ground truth images when the PSF's used for deconvolution were rotated by random angles relative to the PSF's used to create the input images.

SUPPLEMENTARY FIGURE 10 — Variation of PSF across the light sheet in SPIM acquisitions



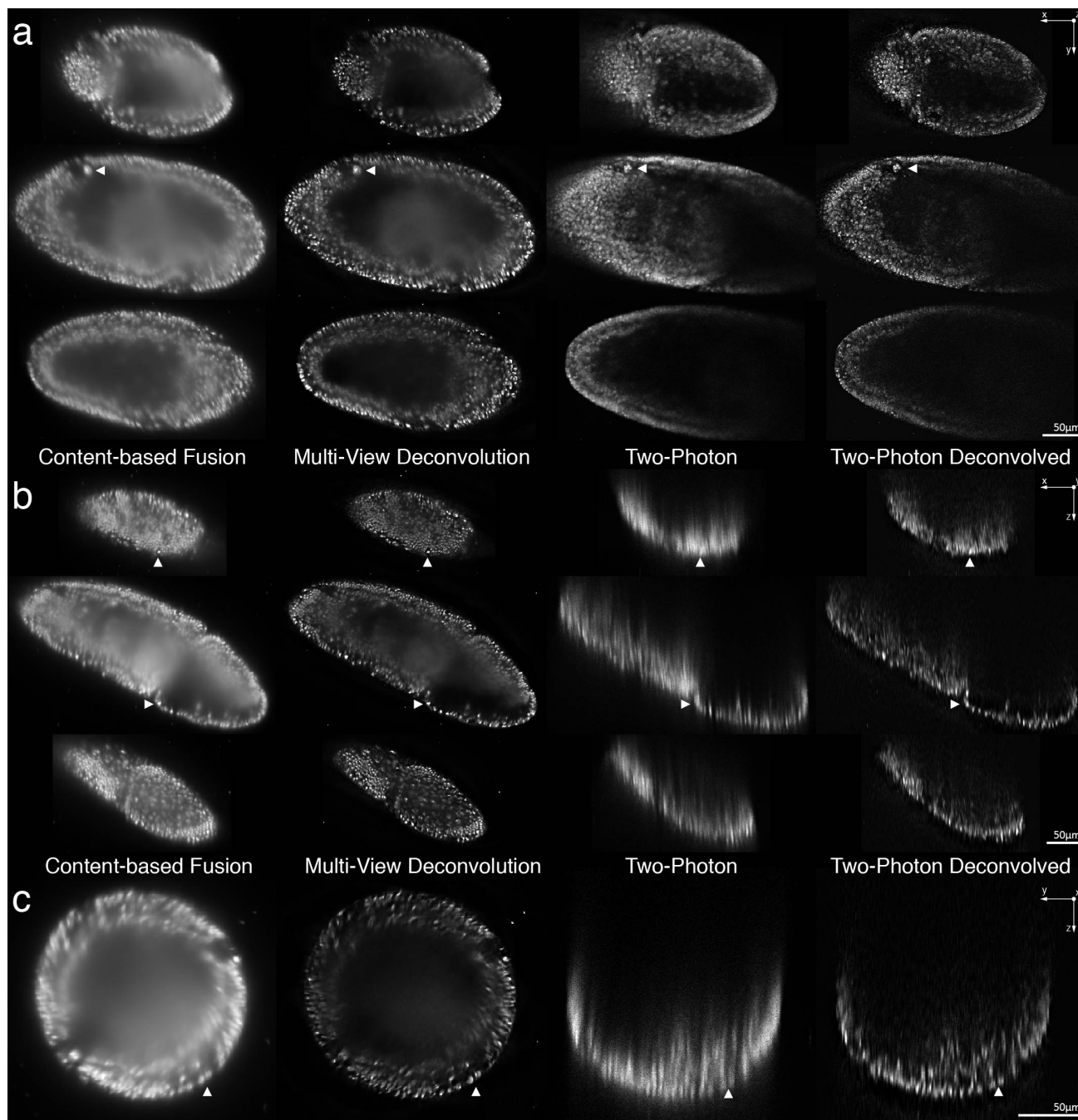
Supplementary Figure 10: Variation of the PSF across the light sheet in SPIM acquisitions. The maximum intensity projection perpendicular to the light sheet of a *Drosophila* embryo expressing His-YFP in all nuclei. The fluorescent beads have a diameter of 500nm. The arrow shows the illumination direction of the light sheet. The fluorescent beads should reflect the concave shape of a light sheet. The red box illustrates the area that is approximately used for deconvolution.

SUPPLEMENTARY FIGURE 11 — Comparison of Multi-View Deconvolution to Structured Illumination Light Sheet Data



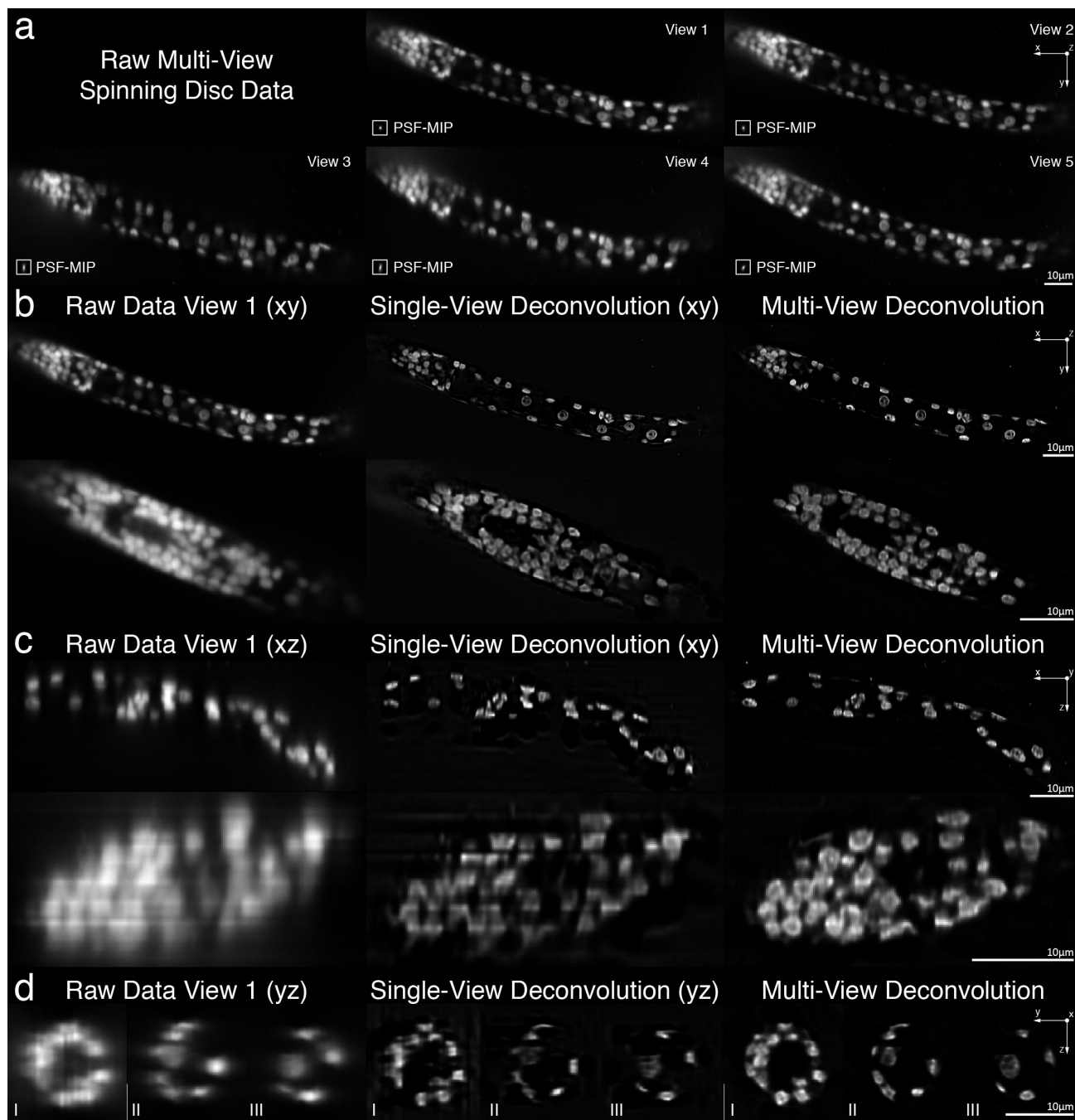
Supplementary Figure 11: Comparison of Multi-View Deconvolution to Structured Illumination Light Sheet Data. (a) Slice through a *Drosophila* embryo expressing a nuclear marker acquired with DSLM and structured illumination (SI). (b) Corresponding slice acquired with standard light sheet microscopy. (a) and (b) taken from Keller et al.¹⁶ (c-j) Slice through a *Drosophila* embryo in a similar stage of embryonic development expressing His-YFP. (c) shows the result of the multi-view deconvolution, (d) the result of the content-based fusion and (e-j) shows a slice through the aligned¹⁴ raw data as acquired by the Zeiss demonstrator B.

SUPPLEMENTARY FIGURE 12 — Comparison of Multi-View Deconvolution to 2p Microscopy



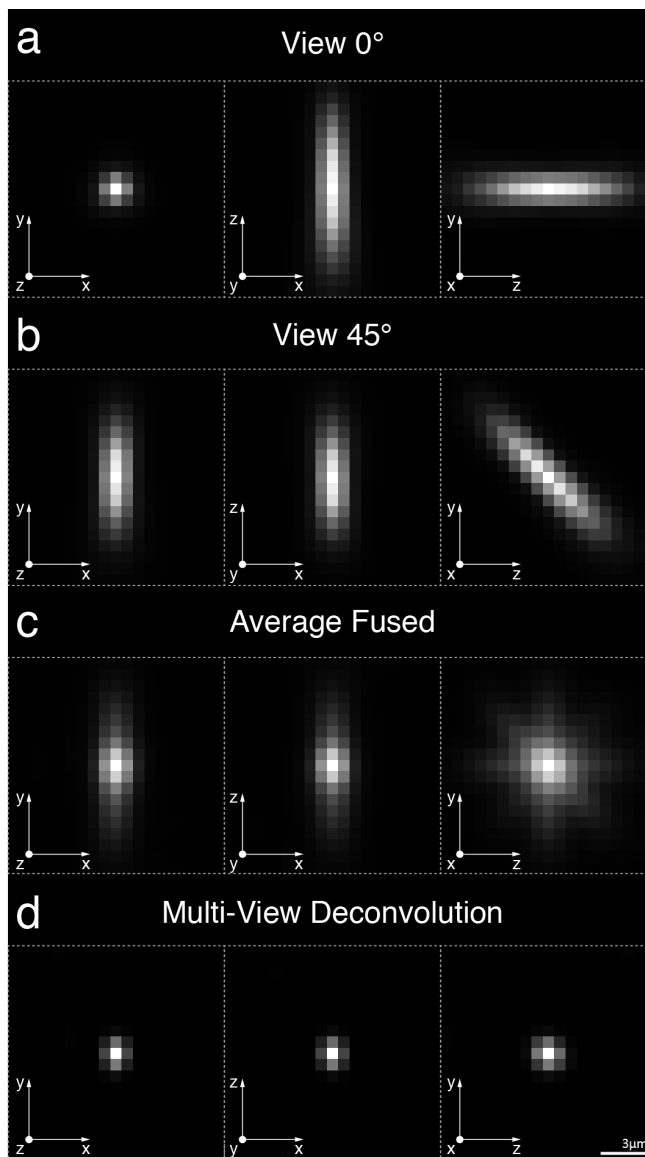
Supplementary Figure 12: Comparing multi-view deconvolution to two-photon (2p) microscopy. (a-c) slices through a fixed Drosophila embryo stained with Sytox green labeling nuclei. Same specimen was acquired with the Zeiss SPIM prototype (20x/0.5NA water dipping obj.) and directly afterwards with a 2p microscope (20x/0.8NA air obj.). We compare the quality of content-based fusion, multi-view deconvolution, raw 2p stack and single view deconvolution of the 2p acquisition. (a) lateral (xy), (b) axial (xz), (c) axial (yz) orientation of the 2p stack, SPIM data is aligned relative to it using the beads in the agarose. Arrows mark corresponding nuclei.

SUPPLEMENTARY FIGURE 13 — Multi-View Deconvolution of Spinning-Disc Confocal Data



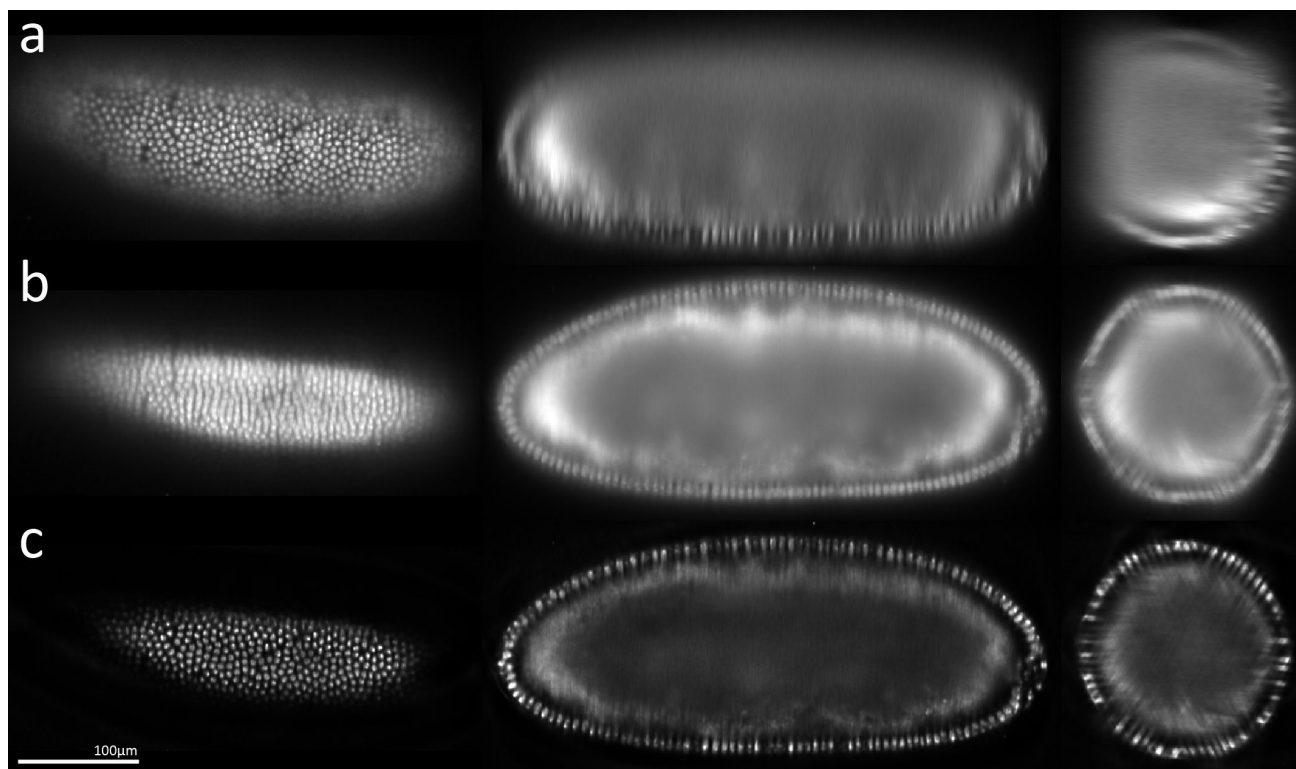
Supplementary Figure 13: Multi-View Deconvolution of a Spinning-Disc Confocal Dataset. (a-d) show slices through a fixed *C. elegans* in L1 stage stained with Sytox green labeling nuclei. The specimen was acquired on a spinning disc confocal microscope (20x/0.5NA water dipping objective). The sample was embedded in agarose and rotated using a self-build device.¹⁴ (a) Slice through the aligned input views; insets show averaged MIP of the PSF. (b-d) slices with different orientations through the larva comparing the quality of the first view of the input data, the single-view deconvolution of view 1 and the multi-view deconvolution of the entire dataset.

SUPPLEMENTARY FIGURE 14 — Quantification of resolution enhancement by Multi-View Deconvolution



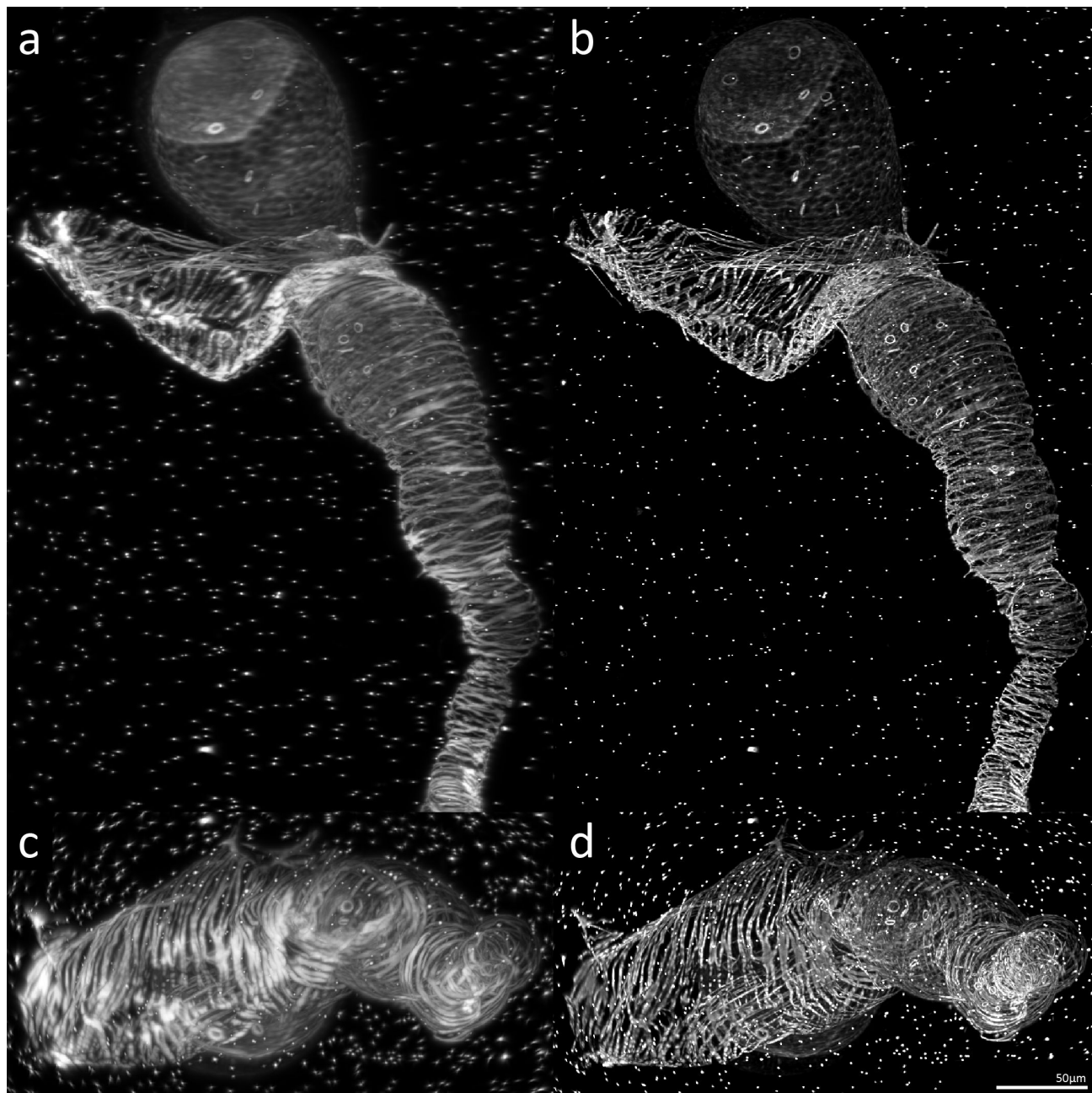
Supplementary Figure 14: Quantification of resolution enhancement by Multi-View Deconvolution. (a-d) compare the average of all fluorescent beads matched by the bead-based registration¹⁴ for two input views (a,b), after multi-view fusion (c), and after multi-view deconvolution (d). The resolution enhancement is apparent, especially along the rotation axis (third column, yz) between (c) and (d). The dataset used for this analysis is the 7-view acquisition of a developing Drosophila embryo (see main text figure 3c-e), deconvolved for 15 iterations with $\lambda=0.0006$ using Optimization I.

SUPPLEMENTARY FIGURE 15 — Reconstruction quality of an OpenSPIM acquisition



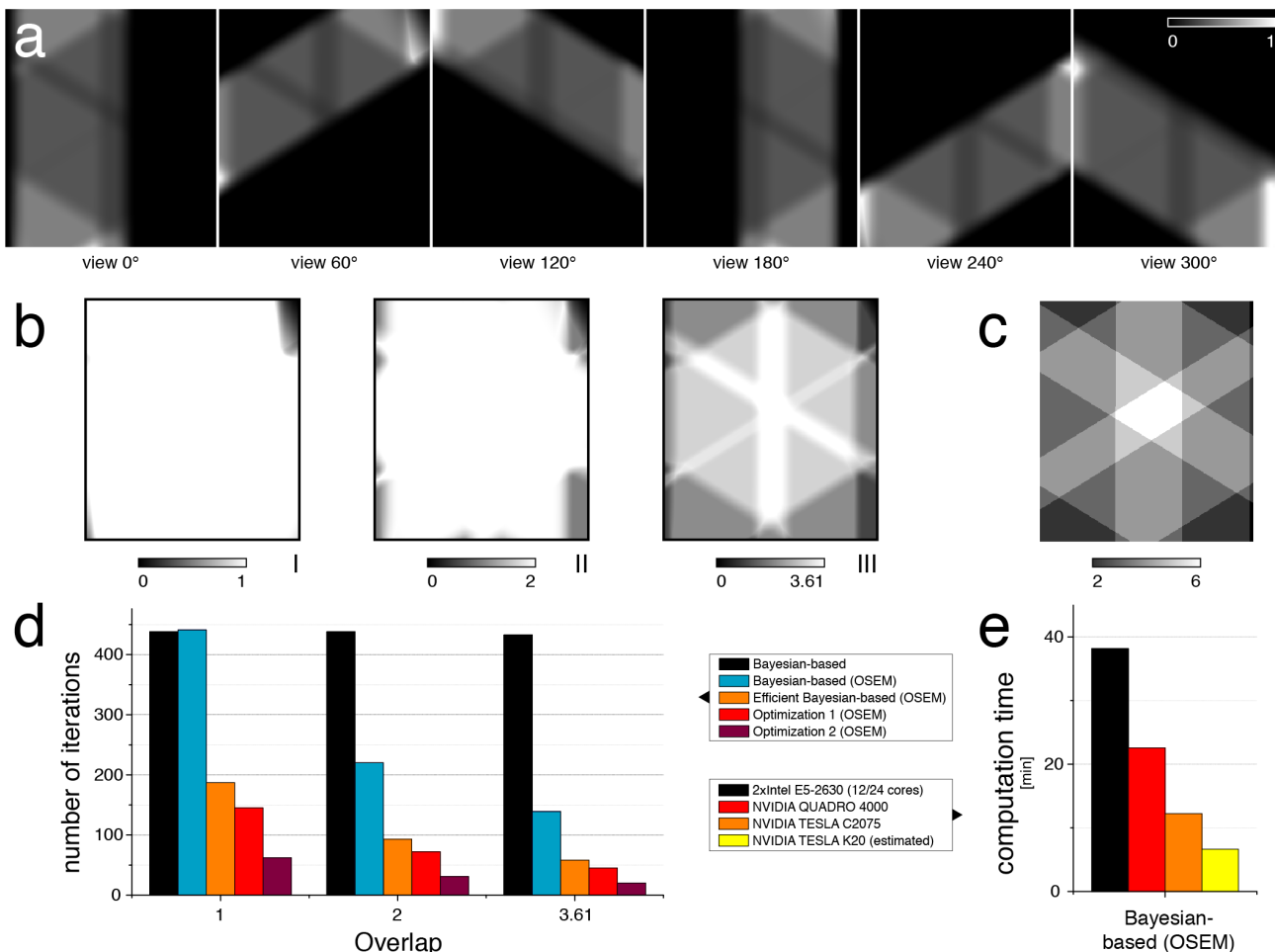
Supplementary Figure 15: Comparison of reconstruction quality on the OpenSPIM. (a) Quality of one of the input views as acquired by the OpenSPIM microscope. (b) Quality of the content-based fusion of the registered dataset. (c) Quality of the deconvolution of the registered dataset. (a-c) The first column shows a slice in the lateral orientation of the input dataset, the second column shows an orthogonal slice, the third column shows a slice perpendicular to the rotation axis. All slices are in the exactly same position and show the identical portion of each volume and are directly comparable. The light sheet thickness of the OpenSPIM is larger than of Zeiss prototype, therefore more out-of-focus light is visible and (a,b) are more blurred. Therefore the effect of deconvolution is especially visible, most dominantly in the third column showing the slice perpendicular to the rotation axis. The dataset has a size of $793 \times 384 \times 370$ px, acquired with in 6 views totalling around 680 million pixels and 2.6 gigabytes of data. Computation time for 12 iterations was 12 minutes on two Nvidia Quadro 4000 GPU's using optimization I.

SUPPLEMENTARY FIGURE 16 — Quality of reconstruction of *Drosophila* ovaries



*Supplementary Figure 16: Comparison of reconstruction quality of *Drosophila* ovaries acquired on the Zeiss SPIM prototype using maximum intensity projections. (a) shows the content-based fusion along the orientation of one of the acquired views. (b) shows the same image deconvolved. (c) shows the projection along the rotation axis of the content-based fusion, (d) of the deconvolved dataset. The final dataset has a size of $822 \times 1211 \times 430$ px, acquired in 12 views totalling an input size of around 5 billion pixels and 19 gigabytes of data (32 bit floating point data required for deconvolution). Computation time for 12 iterations was 36 minutes on two Nvidia Quadro 4000 GPU's using optimization I.*

SUPPLEMENTARY FIGURE 17 — Effects of partial overlap and CUDA performance



Supplementary Figure 17: Effects of partial overlap and CUDA performance. **(a)** shows for one slice perpendicular to the rotation axis the weights for each pixel of each view of a six-view SPIM acquisition (see supplementary figure 11 e-j for image data). Every view only covers part of the entire volume. Close to the boundaries of each view we limit its contribution using a cosine blending function preventing artifacts due to sharp edges.¹⁴ For each individual pixel the sum of weights over all views is normalized to be ≤ 1 . Black corresponds to a weight of 0 (this view is not contributing), white to a weight of 1 (only this view is contributing). **(b)** illustrates how much each pixel is deconvolved in every iteration when using different amounts of OSEM speedup (i.e. assuming a certain amount of overlapping views). Note that individual weights must not be > 1 . **(b-I)** normalizing the sum of all weights to ≤ 1 results in a uniformly deconvolved image except the corners where the underlying data is missing, however no speedup is achieved by OSEM (**d** left). Note that summing up all 6 images from **(a)** results in this image. **(b-II)** two views is the minimal number of overlapping views at every pixel (see **c**), so normalization to ≤ 2 still provides a pretty uniform deconvolution and a 2-fold speed up (**d** center). **(b-III)** normalizing to ≤ 3.61 (average number of overlapping views) results in more deconvolution of center parts, which is not desirable. Many parts of the image are not covered by enough views to achieve a sum of weights of 3.61. **(d)** performance improvement of partially overlapping datasets using the weights pictured above and a cropped version of the ground truth image (supplementary figure 5). The effect is identical to perfectly overlapping views, but the effective number of overlapping views is reduced. Our new optimizations improve performance in any case. **(e)** the relative speed-up of deconvolution performance that can be achieved using our CUDA implementation.

SUPPLEMENTARY TABLES

SUPPLEMENTARY TABLE 1 — Summary of datasets used in this publication

Dataset	Size, Lightsheet Thickness, SNR*	Computation Time, Iterations, Method	Machine
<i>Drosophila</i> embryo expressing His-YFP in all cells acquired with Zeiss SPIM prototype using a 20x/0.5 detection objective (Fig. 2c-e, Supp. Fig. 14) [†]	720×380×350 px, 7 views, LS~5μm, SNR~30	7 minutes, 12 iterations, optimization I, λ = 0.006	2× Nvidia Quadro 4000 [‡] , 64 GB RAM
<i>Drosophila</i> embryo expressing His-YFP in all cells acquired with the Open-SPIM using a 20x/0.5 detection objective (Supp. Fig. 15)	793×384×370 px, 6 views, LS~10μm, SNR~15	12 minutes [§] , 12 iterations, optimization I, λ = 0.006	2× Nvidia Quadro 4000 [‡] , 64 GB RAM
<i>Drosophila</i> ovaries acquired on the Zeiss SPIM prototype using a 20x/0.5 detection objective (Supp. Fig. 16)	1211×822×430 px, 12 views, LS~5μm, SNR~19	36 minutes, 12 iterations, optimization I, λ = 0.006	2× Nvidia Quadro 4000 [‡] , 64 GB RAM
<i>Drosophila</i> embryo expressing His-YFP in all cells acquired with Zeiss SPIM prototype using a 20x/0.5 detection objective (Supp. Video 2-4, Supp. Fig. 11)	792×320×310 px, 6 views, 236 timepoints, LS~5μm, SNR~26	24.3 hours, 12 iterations, optimization I, λ = 0.006	2× Nvidia Quadro 4000 [‡] , 64 GB RAM
<i>Drosophila</i> embryo expressing Histone-H2Av-mRFP _{ruby} fusion in all cells imaged on Zeiss Lightsheet Z1 with a 20x/1.0 detection objective and dual-sided illumination	928×390×390 px, 6 views, 715 timepoints, LS~5μm, SNR~21	35 hours, 10 iterations, optimization I, λ = 0.0006	4× Nvidia TESLA [¶] , 64 GB RAM
<i>C. elegans</i> embryo in 4-cell stage expressing PH-domain-GFP fusion acquired with Zeiss SPIM prototype using a 40x/0.8 detection objective (Fig. 2a,b) [†]	180×135×180 px, 6 views, LS~3.5μm, SNR~40	1 minute, 20 iterations, optimization I, λ = 0.006	2× Intel Xeon E5-2630, 64 GB RAM
Fixed <i>C. elegans</i> larvae in L1 stage expressing LMN-1::GFP and stained with Hoechst imaged on Zeiss Lightsheet Z1 with a 20x/1.0 detection objective (Fig. 2f,g and Supp. Video 5-8)	1640×1070×345 px, 4 views, 2 channels, LS~2μm, SNR~62 (Hoechst), SNR~24 (GFP)	2×160 minutes, 100 iterations, optimization II, λ = 0	2× Intel Xeon E5-2690, 128 GB RAM

*The SNR is estimated by computing the average intensity of the signal, divided by the standard deviation of the signal in areas with homogenous sample intensity

[†]This SPIM acquisition was already used in Preibisch (2010)¹⁴ to illustrate the results of the bead-based registration and multi-view fusion; we use the underlying dataset again to illustrate the improved results of the multi-view deconvolution.

[‡]Two graphics cards in one PC, which can process two 512×512×512 blocks in parallel

[§]Note that the increased computation time is due to larger anisotropy of the acquired stacks leading to larger effective

SUPPLEMENTARY TABLE 1 (CONTINUED) — Summary of datasets used in this publication

Dataset	Size, Lightsheet Thickness, SNR	Computation Time, Iterations, Method	Machine
Fixed <i>C. elegans</i> in L1 stage stained with Sytox green acquired with Spinning Disc Confocal using a 20x/0.5 detection objective (Supp. Fig. 13) [¶]	1135×400×430 px, 5 views, LS N/A, SNR~28	36 minutes, 50 iterations, optimization II, $\lambda = 0.0006$	2× Intel Xeon E5-2680, 128 GB RAM
Fixed <i>C. elegans</i> in L1 stage stained with Sytox green acquired with Spinning Disc Confocal using a 20x/0.5 detection objective (Supp. Fig. 13) ^{**}	1151×426×190 px, 1 view, LS N/A, SNR~28	202 minutes, 900 iterations, Lucy-Richardson , $\lambda = 0.0006$	2× Intel Xeon E5620, 64 GB RAM
Fixed <i>Drosophila</i> embryo stained with Sytox green acquired on the Zeiss SPIM prototype using a 20x/0.5 detection objective (Supp. Fig. 12)	642×316×391 px, 9 views, LS~5 μ m, SNR~20	15 minutes, 15 iterations, optimization I, $\lambda = 0.006$	2× Intel Xeon E5-2680, 128 GB RAM
Fixed <i>Drosophila</i> embryo stained with Sytox green acquired on a Two-Photon Microscope using a 20x/0.8 detection objective (Supp. Fig. 12)	856×418×561 px, 1 view, LS N/A, SNR~7	160 minutes, 300 iterations, Lucy-Richardson , $\lambda = 0.006$	2× Intel Xeon E5620, 64 GB RAM

*Supplementary Table 1: Summary of all datasets used in this publication. Note that the multi-view deconvolution of the *C. elegans* larvae in L1 stage (SPIM & Spinning Disc Confocal) required an additional registration step, which is explained in section 15.*

PSF sizes, which increases computational effort. The image could therefore not be split up into two 512×512×512 blocks.

[¶]Run on a cluster with 4 nodes that are equipped with one Nvidia TESLA and 64 GB of system memory

^{¶¶}This multi-view spinning disc acquisition was already used in Preibisch (2010)¹⁴ to illustrate the applicability of the bead-based registration and multi-view fusion to other technologies than SPIM; we use the underlying dataset again to illustrate the improved results and applicability of the multi-view deconvolution.

^{**}This is the same dataset as in the row above, but showing the time it took to compute the single-view deconvolution.

SUPPLEMENTARY NOTE

1. REMARKS

This document closely follows the notation introduced in the paper of L. B. Lucy¹² whenever possible. Note that for simplicity the derivations in this document only cover the one dimensional case. Nevertheless, all equations are valid for any n -dimensional case.

2. BAYESIAN-BASED SINGLE-VIEW DECONVOLUTION

This section re-derives the classical bayesian-based Richardson¹¹-Lucy¹² deconvolution for single images, other derivations presented in this document build up on it. The goal is to estimate the frequency distribution of an underlying signal $\psi(\xi)$ from a finite number of measurements $x^{1'}, x^{2'}, \dots, x^{N'}$. The resulting observed distribution $\phi(x)$ is defined as

$$\phi(x) = \int_{\xi} \psi(\xi) P(x|\xi) d\xi \quad (3)$$

where $P(x|\xi)$ is the probability of a measurement occurring at $x = x'$ when it is known that the event $\xi = \xi'$ occurred. In more practical image analysis terms equation 3 describes the one-dimensional convolution operation where $\phi(x)$ is the blurred image, $P(x|\xi)$ is the kernel and $\psi(\xi)$ is the undegraded (or deconvolved) image. All distributions are treated as probability distributions and fulfill the following constraints:

$$\int_{\xi} \psi(\xi) d\xi = \int_x \phi(x) dx = \int_x P(x|\xi) dx = 1 \quad \text{and} \quad \psi(\xi) > 0, \phi(x) \geq 0, P(x|\xi) \geq 0 \quad (4)$$

2.1 Derivation of the iterative deconvolution scheme

The basis for the derivation of the bayesian-based deconvolution is the tautology

$$P(\xi = \xi' \wedge x = x') = P(x = x' \wedge \xi = \xi') \quad (5)$$

It states that it is equally probable that the event ξ' results in a measurement at x' and that the measurement at x' was caused by the event ξ' . Integrating equation 5 over the measured distribution yields the joint probability distribution

$$\int_x P(\xi \wedge x) dx = \int_x P(x \wedge \xi) dx \quad (6)$$

which can be expressed using conditional probabilities

$$\int_x P(\xi) P(x|\xi) dx = \int_x P(x) P(\xi|x) dx \quad (7)$$

and in correspondence to Lucy's notation looks like (equation 3)

$$\int_x \psi(\xi) P(x|\xi) dx = \int_x \phi(x) Q(\xi|x) dx \quad (8)$$

where $P(\xi) \equiv \psi(\xi)$, $P(x) \equiv \phi(x)$, $P(\xi|x) \equiv Q(\xi|x)$. $Q(\xi|x)$ denotes what Lucy calls the 'inverse' conditional probability to $P(x|\xi)$. It defines the probability that an event at ξ' occurred, given a specific measurement at x' . As $\psi(\xi)$ does not depend on x , equation 8 can be rewritten as

$$\psi(\xi) \overbrace{\int_x P(x|\xi) dx}^{=1} = \int_x \phi(x) Q(\xi|x) dx \quad (9)$$

hence (due to equation 4)

$$\psi(\xi) = \int_x \phi(x)Q(\xi|x)dx \quad (10)$$

which corresponds to the inverse of the convolution in equation 3. Although $Q(\xi|x)$ cannot be used to directly compute $\psi(\xi)$, *Bayes' Theorem* and subsequently equation 3 can be used to reformulate it as

$$Q(\xi|x) = \frac{\psi(\xi)P(x|\xi)}{\phi(x)} = \frac{\psi(\xi)P(x|\xi)}{\int_{\xi} \psi(\xi)P(x|\xi)d\xi} \quad (11)$$

Replacing $Q(\xi|x)$ in equation 10 yields

$$\psi(\xi) = \int_x \phi(x) \frac{\psi(\xi)P(x|\xi)}{\int_{\xi} \psi(\xi)P(x|\xi)d\xi} dx = \psi(\xi) \int_x \frac{\phi(x)}{\int_{\xi} \psi(\xi)P(x|\xi)d\xi} P(x|\xi) dx \quad (12)$$

which exactly re-states the deconvolution scheme introduced by Lucy and Richardson. The fact that both sides of the equation contain the desired underlying (deconvolved) distribution $\psi(\xi)$ suggests an iterative scheme to converge towards the correct solution

$$\psi^{r+1}(\xi) = \psi^r(\xi) \int_x \frac{\phi(x)}{\int_{\xi} \psi^r(\xi)P(x|\xi)d\xi} P(x|\xi) dx \quad (13)$$

where $\psi^0(\xi)$ is simply a constant distribution with each value being the average intensity of the measured distribution $\phi(x)$.

Equation 13 turns out to be a maximum-likelihood (ML) expectation-maximization (EM) formulation,¹³ which works as follows. First, it computes for every pixel the convolution of the current guess of the deconvolved image $\psi^r(\xi)$ with the kernel (PSF) $P(x|\xi)$, i.e. $\phi^r(x) = \int_{\xi} \psi^r(\xi)P(x|\xi)d\xi$. In EM-terms $\phi^r(x)$ describes the *expected value*. The quotient between the input image $\phi(x)$ and the *expected value* $\phi^r(x)$ yields the disparity for every pixel. These values are initially large but will become very small upon convergence. In an ideal scenario all values of $\phi^r(x)$ and $\phi(x)$ will be identical once the algorithm converged. This ratio is subsequently convolved with the point spread function $P(x|\xi)$ reflecting which pixels influence each other. In EM-terms this is called the *maximization step*. This also preserves smoothness. These resulting values are then pixel-wise multiplied with the current guess of the deconvolved image $\psi^r(\xi)$, which we call an RL-update (Richardson-Lucy). It results in a new guess for the deconvolved image.

Starting from an initial guess of an image with constant values, this scheme will converge towards the correct solution if the guess of the point spread function is correct and if the observed distribution is not degraded by noise, transformations, etc.

2.1.1 Integrating ξ and x

Note that convolution of $\psi^r(\xi)$ with $P(x|\xi)$ requires integration over ξ , while the convolution of the quotient image with $P(x|\xi)$ integrates over x . Integration over x can be formulated as convolution if $P(x|\xi)$ is constant by using inverted coordinates $P(-x|\xi)$. Note that it can be ignored if the kernel is symmetric $P(x|\xi) = P(-x|\xi)$. For single-view datasets this is often the case, whereas multi-view datasets typically have non-symmetric kernels due to their transformations resulting from image alignment.

3. BAYESIAN-BASED MULTI-VIEW DECONVOLUTION

This section shows for the first time the entire derivation of bayesian-based multi-view deconvolution using probability theory. Compared to the single-view case we have a set of views $V = \{v_1 \dots v_N : N = |V|\}$ comprising N observed distributions $\phi_v(x_v)$ (input views acquired from different angles), N point spread functions $P_v(x_v|\xi)$

corresponding to each view, and one underlying signal distribution $\psi(\xi)$ (deconvolved image). The observed distributions $\phi_v(x_v)$ are accordingly defined as

$$\phi_1(x_1) = \int_{\xi} \psi(\xi)P(x_1|\xi)d\xi \quad (14)$$

$$\phi_2(x_2) = \int_{\xi} \psi(\xi)P(x_2|\xi)d\xi \quad (15)$$

$$\dots \quad (16)$$

$$\phi_N(x_N) = \int_{\xi} \psi(\xi)P(x_N|\xi)d\xi \quad (17)$$

The basis for the derivation of the bayesian-based multi-view deconvolution is again a tautology based on the individual observations

$$P(\xi = \xi' \wedge x_1 = x'_1 \wedge \dots \wedge x_N = x'_N) = P(x_1 = x'_1 \wedge \dots \wedge x_N = x'_N \wedge \xi = \xi') \quad (18)$$

Integrating equation 18 over the measured distributions yields the joint probability distribution

$$\int_{x_1} \dots \int_{x_N} P(\xi \wedge x_1 \wedge \dots \wedge x_N)dx_1 \dots dx_N = \int_{x_1} \dots \int_{x_N} P(x_1 \wedge \dots \wedge x_N \wedge \xi)dx_1 \dots dx_N \quad (19)$$

shortly written as

$$\int_{\bar{x}} P(\xi, x_1, \dots, x_N)d\bar{x} = \int_{\bar{x}} P(x_1, \dots, x_N, \xi)d\bar{x} \quad (20)$$

By expressing the term using conditional probabilities one obtains

$$\int_{\bar{x}} P(\xi)P(x_1|\xi)P(x_2|\xi, x_1) \dots P(x_N|\xi, x_1, \dots, x_{N-1})d\bar{x} = \int_{\bar{x}} P(x_1)P(x_2|x_1)P(x_3|x_1, x_2) \dots P(\xi|x_1, \dots, x_N)d\bar{x} \quad (21)$$

On the left side of the equation all terms are conditionally independent of any x_v given ξ . This results from the fact that if an event $\xi = \xi'$ occurred, each individual measurement x_v depends only on ξ' and the respective point spread function $P(x_v|\xi)$ (supplementary figure 1a for illustration). Equation 21 therefore reduces to

$$P(\xi) \overbrace{\int_{\bar{x}} P(x_1|\xi)P(x_2|\xi) \dots P(x_N|\xi)d\bar{x}}^{=1} = \int_{\bar{x}} P(x_1)P(x_2|x_1)P(x_3|x_1, x_2) \dots P(x_N|x_1, \dots, x_{N-1})P(\xi|x_1, \dots, x_N)d\bar{x} \quad (22)$$

Assuming independence of the observed distributions $P(x_v)$ equation 22 further simplifies to

$$P(\xi) = \int_{\bar{x}} P(x_1)P(x_2)P(x_3) \dots P(x_N)P(\xi|x_1, \dots, x_N)d\bar{x} \quad (23)$$

Although independence between the views is assumed,^{9,10,21} the underlying distribution $P(\xi)$ still depends on the observed distributions $P(x_v)$ through $P(\xi|x_1, \dots, x_N)$.

Note: In section 5 we will show that that the derivation of bayesian-based multi-view deconvolution can be achieved without assuming independence of the observed distributions $P(x_v)$. Based on that derivation we argue that there is a relationship between the $P(x_v)$'s (supplementary figure 1b for illustration) and that it can be incorporated into the derivation to achieve faster convergence as shown in sections 7 and 8.

We cannot approximate $P(\xi|x_1, \dots, x_N)$ directly and therefore need to reformulate it in order to express it using individual $P(\xi|x_v)$, which can subsequently be used to formulate the deconvolution task as shown in section 2. Note that according to Lucy's notation $P(\xi|x_1, \dots, x_N) \equiv Q(\xi|x_1, \dots, x_N)$ and $P(\xi|x_v) \equiv Q(\xi|x_v)$.

$$P(\xi|x_1, \dots, x_N) = \frac{P(\xi, x_1, \dots, x_N)}{P(x_1, \dots, x_N)} \quad (24)$$

$$P(\xi|x_1, \dots, x_N) = \frac{P(\xi)P(x_1|\xi)P(x_2|\xi, x_1) \dots P(x_N|\xi, x_1, \dots, x_{N-1})}{P(x_1)P(x_2|x_1) \dots P(x_N|x_1, \dots, x_{N-1})} \quad (25)$$

Due to the conditional independence of the $P(x_v)$ given ξ (equation 21 → 22 and supplementary figure 1a) and the assumption of independence between the $P(x_v)$ (equation 22 → 23) equation 25 simplifies to

$$P(\xi|x_1, \dots, x_N) = \frac{P(\xi)P(x_1|\xi)\dots P(x_N|\xi)}{P(x_1)\dots P(x_N)} \quad (26)$$

Using *Bayes' Theorem* to replace all

$$P(x_v|\xi) = \frac{P(x_v)P(\xi|x_v)}{P(\xi)} \quad (27)$$

yields

$$P(\xi|x_1, \dots, x_N) = \frac{P(\xi) P(\xi|x_1)P(x_1)\dots P(\xi|x_N)P(x_N)}{P(x_1)\dots P(x_N) P(\xi)^N} \quad (28)$$

$$P(\xi|x_1, \dots, x_N) = \frac{P(\xi) P(\xi|x_1)\dots P(\xi|x_N)}{P(\xi)^N} \quad (29)$$

$$P(\xi|x_1, \dots, x_N) = \frac{P(\xi|x_1)\dots P(\xi|x_N)}{P(\xi)^{N-1}} \quad (30)$$

Substituting equation 30 in equation 23 yields

$$P(\xi) = \frac{\int_{\bar{x}} P(x_1) \dots P(x_N) P(\xi|x_1)\dots P(\xi|x_N) d\bar{x}}{P(\xi)^{N-1}} \quad (31)$$

and rewritten in Lucy's notation

$$\psi(\xi) = \frac{\int_{\bar{x}} \phi_1(x_1) \dots \phi_N(x_N) Q(\xi|x_1)\dots Q(\xi|x_N) d\bar{x}}{\psi(\xi)^{N-1}} \quad (32)$$

$$\psi(\xi) = \frac{\int_{x_1} \phi_1(x_1) Q(\xi|x_1) dx_1 \dots \int_{x_N} \phi_N(x_N) Q(\xi|x_N) dx_N}{\psi(\xi)^{N-1}} \quad (33)$$

$$\psi(\xi) = \frac{\prod_{v \in V} \int_{x_v} \phi_v(x_v) Q(\xi|x_v) dx_v}{\psi(\xi)^{N-1}} \quad (34)$$

As in the single view case we replace $Q(\xi|x_v)$ with equation 11

$$\psi(\xi) = \frac{\prod_{v \in V} \int_{x_v} \phi_v(x_v) \frac{\psi(\xi) P(x_v|\xi)}{\int_{\xi} \psi(\xi) P(x_v|\xi) d\xi} dx_v}{\psi(\xi)^{N-1}} \quad (35)$$

$$\psi(\xi) = \frac{\psi(\xi) \prod_{v \in V} \int_{x_v} \phi_v(x_v) \frac{P(x_v|\xi)}{\int_{\xi} \psi(\xi) P(x_v|\xi) d\xi} dx_v}{\cancel{\psi(\xi)^{N-1}}} \quad (36)$$

$$\psi(\xi) = \psi(\xi) \prod_{v \in V} \int_{x_v} \phi_v(x_v) \frac{P(x_v|\xi)}{\int_{\xi} \psi(\xi) P(x_v|\xi) d\xi} dx_v \quad (37)$$

As in the single view case, both sides of the equation contain the desired deconvolved distribution $\psi(\xi)$. This again suggests the final iterative scheme

$$\psi^{r+1}(\xi) = \psi^r(\xi) \prod_{v \in V} \int_{x_v} \frac{\phi_v(x_v)}{\int_{\xi} \psi^r(\xi) P(x_v|\xi) d\xi} P(x_v|\xi) dx_v \quad (38)$$

where $\psi^0(\xi)$ is considered a distribution with a constant value. Note that the final derived equation 38 ends up being the per pixel multiplication of the single view RL-updates from equation 13.

It is important to note that the maximum-likelihood expectation-maximization based derivation⁵ yields an additive combination of the individual RL-updates, while our derivation based probability theory and *Bayes' Theorem* ends up being a multiplicative combination. However, our derivation enables us to prove (section 5) that this formulation can be achieved without assuming independence of the observed distributions (input views), which allows us to introduce optimizations to the derivation (sections 7 and 8). We additionally proof in section 4 the convergence of our multiplicative derivation to the maximum-likelihood solution.

4. PROOF OF CONVERGENCE

This section proofs that our Bayesian-based derivation of multi-view deconvolution (equation 38) converges to the maximum-likelihood (ML) solution using noise-free data. We chose to adapt the proof developed for *Ordered Subset Expectation Maximization* (OS-EM)⁶ due to its similarity to our derivation (see section 9).

4.1 PROOF FOR NOISE-FREE DATA

Assuming the existence of a feasible solution ψ^* it has been shown⁶ that the likelihood $L^r := L(\psi^r; \psi^*)$ of the solution ψ at iteration r can be computed as

$$L(\psi^r; \psi^*) = - \int_{\xi} \psi^*(\xi) \log \frac{\psi^*(\xi)}{\psi^r(\xi)} d\xi \quad (39)$$

Following the argumentations of Shepp and Vardi,⁵ Kaufmann²² and Hudson and Larkin⁶ convergence of the algorithm is proven if the likelihood of the solution ψ increases with every iteration since L is bounded by 0. In other words

$$\Delta L = L^{r+1} - L^r \quad (40)$$

$$\geq 0 \quad (41)$$

We will now prove that ΔL is indeed always greater or equal to zero. Replacing equation 39 in equation 40 yields

$$\Delta L = \int_{\xi} \psi^*(\xi) \log \frac{\psi^*(\xi)}{\psi^r(\xi)} - \psi^*(\xi) \log \frac{\psi^*(\xi)}{\psi^{r+1}(\xi)} d\xi \quad (42)$$

$$= \int_{\xi} \psi^*(\xi) \log \frac{\psi^{r+1}(\xi)}{\psi^r(\xi)} d\xi \quad (43)$$

Next, we substitute $\psi^{r+1}(\xi)$ with our derivation of Bayesian-based multi-view deconvolution (equation 38). Note that for simplicity we replace $\int_{\xi} \psi^r(\xi) P(x_v|\xi) d\xi$ with $\phi_v^r(x_v)$, which refers to the current estimate of the observed distribution given the current guess of the underlying distribution ψ^r (or in EM terms the *expected value*).

$$\Delta L = \int_{\xi} \psi^*(\xi) \log \frac{\psi^r(\xi) \left(\prod_{v \in V} \int_{x_v} \frac{\phi_v(x_v)}{\phi_v^r(x_v)} P(x_v|\xi) dx_v \right)^{\frac{1}{|V|}}}{\psi^r(\xi)} d\xi \quad (44)$$

$$= \int_{\xi} \psi^*(\xi) \log \left(\prod_{v \in V} \int_{x_v} \frac{\phi_v(x_v)}{\phi_v^r(x_v)} P(x_v|\xi) dx_v \right)^{\frac{1}{|V|}} d\xi \quad (45)$$

$$= \frac{1}{|V|} \sum_{v \in V} \int_{\xi} \psi^*(\xi) \log \int_{x_v} \frac{\phi_v(x_v)}{\phi_v^r(x_v)} P(x_v|\xi) dx_v d\xi \quad (46)$$

As equation 38 expresses a proportion, it is necessary to normalize for the number of observed distributions $|V|$ and apply the $|V|$ 'th root, i.e. compute the geometric mean. Note that this normalization is the equivalent to the division by $|V|$ as applied in the ML-EM derivations^{5,10} that use the arithmetic mean of the individual RL-updates in order to update underlying distribution.

Using Jensen's inequality equation 46 can be reformulated (equation 47) and further simplified

$$\Delta L \geq \frac{1}{|V|} \sum_{v \in V} \int_{\xi} \psi^*(\xi) \int_{x_v} \log \left(\frac{\phi_v(x_v)}{\phi_v^r(x_v)} \right) P(x_v|\xi) dx_v d\xi \quad (47)$$

$$= \frac{1}{|V|} \sum_{v \in V} \int_{x_v} \log \left(\frac{\phi_v(x_v)}{\phi_v^r(x_v)} \right) \int_{\xi} \psi^*(\xi) P(x_v|\xi) d\xi dx_v \quad (48)$$

Substituting equation 3 in equation 48 yields

$$\Delta L \geq \frac{1}{|V|} \sum_{v \in V} \int_{x_v} \log \left(\frac{\phi_v(x_v)}{\phi_v^r(x_v)} \right) \phi_v(x_v) dx_v \quad (49)$$

It follows directly that in order to prove that $\Delta L \geq 0$, it is sufficient to prove that

$$\int_{x_v} \log \left(\frac{\phi_v(x_v)}{\phi_v^r(x_v)} \right) \phi_v(x_v) dx_v \geq 0 \quad (50)$$

Based on the inequality $\log x \geq 1 - x^{-1}$ for $x > 0$ proven by *Adolf Hurwitz*, we need to show that

$$\int_{x_v} \log \left(\frac{\phi_v(x_v)}{\phi_v^r(x_v)} \right) \phi_v(x_v) dx_v \geq \int_{x_v} \left(1 - \frac{\phi_v^r(x_v)}{\phi_v(x_v)} \right) \phi_v(x_v) dx_v \geq 0 \quad (51)$$

$$= \int_{x_v} \phi_v(x_v) dx_v - \int_{x_v} \phi_v^r(x_v) dx_v \quad (52)$$

$$= \int_{x_v} \phi_v(x_v) dx_v - \int_{x_v} \int_{\xi} \psi^r(\xi) P(x_v|\xi) d\xi dx_v \quad (53)$$

$$= \int_{x_v} \phi_v(x_v) dx_v - \int_{\xi} \psi^r(\xi) \overbrace{\int_{x_v} P(x_v|\xi) dx_v}^{=1} d\xi \quad (54)$$

$$= \int_{x_v} \phi_v(x_v) dx_v - \int_{\xi} \psi^r(\xi) d\xi \quad (55)$$

$$\geq 0 \iff \int_{x_v} \phi_v(x_v) dx_v \geq \int_{\xi} \psi^r(\xi) d\xi \quad (56)$$

In other words, convergence is proven if we show that energy of the underlying distribution $\psi(\xi)$ (deconvolved image) is never greater than energy of each observed distribution $\phi_v(x_v)$ (input views). Replacing $\psi^r(\xi)$ with our Bayesian-based derivation (equation 38), shows that proving the condition in equation 56 is equivalent to proving

$$\int_{x_v} \phi_v(x_v) dx_v \geq \int_{\xi} \psi^r(\xi) \left(\prod_{v \in V} \int_{x_v} \frac{\phi_v(x_v)}{\phi_v^r(x_v)} P(x_v|\xi) dx_v \right)^{\frac{1}{|V|}} d\xi \quad (57)$$

Note that as this inequality has to hold for any iteration r , we refrain from writing $r - 1$ for simplicity. As the arithmetic average is always greater or equal than the geometric average²³ it follows that proving equation 57 is equivalent to

$$\int_{x_v} \phi_v(x_v) dx_v \geq \int_{\xi} \psi^r(\xi) \frac{1}{|V|} \sum_{v \in V} \int_{x_v} \frac{\phi_v(x_v)}{\phi_v^r(x_v)} P(x_v|\xi) dx_v d\xi \geq \int_{\xi} \psi^r(\xi) \left(\prod_{v \in V} \int_{x_v} \frac{\phi_v(x_v)}{\phi_v^r(x_v)} P(x_v|\xi) dx_v \right)^{\frac{1}{|V|}} d\xi \quad (58)$$

and we therefore need to prove the inequality only for the arithmetic average. We simplify equation 58 as follows

$$\int_{x_v} \phi_v(x_v) dx_v \geq \frac{1}{|V|} \sum_{v \in V} \int_{\xi} \psi^r(\xi) \int_{x_v} \frac{\phi_v(x_v)}{\phi_v^r(x_v)} P(x_v|\xi) dx_v d\xi \quad (59)$$

$$= \frac{1}{|V|} \sum_{v \in V} \int_{x_v} \frac{\phi_v(x_v)}{\phi_v^r(x_v)} \int_{\xi} \psi^r(\xi) P(x_v|\xi) d\xi dx_v \quad (60)$$

$$= \frac{1}{|V|} \sum_{v \in V} \int_{x_v} \frac{\phi_v(x_v)}{\phi_v^r(x_v)} \phi_v^r(x_v) dx_v \quad (61)$$

$$= \frac{1}{|V|} \sum_{v \in V} \int_{x_v} \phi_v(x_v) dx_v \quad (62)$$

As the integral of all input views is identical (equation 4), equation 62 is always true, and we proved that our Bayesian-based derivation of multi-view deconvolution always converges to the Maximum Likelihood.

5. DERIVATION OF BAYESIAN-BASED MULTI-VIEW DECONVOLUTION WITHOUT ASSUMING INDEPENDENCE OF THE VIEWS

Previous derivations of the Richardson-Lucy multi-view deconvolution^{5,9,10,21} assumed independence of the individual views in order to derive variants of equation 38. The following derivation shows that it is actually not necessary to assume independence of the observed distributions $\phi_v(x_v)$ (equation 22 \rightarrow 23 and equation 25 \rightarrow 26) in order to derive the formulation for bayesian-based multi-view deconvolution shown in equation 38.

We therefore rewrite equation 23 without assuming independence (which is then identical to equation 22) and obtain

$$P(\xi) = \int_{\bar{x}} P(x_1)P(x_2|x_1) \dots P(x_N|x_1, \dots, x_{N-1})P(\xi|x_1, \dots, x_N) d\bar{x} \quad (63)$$

We consequently also do not assume independence in equation 26, which intends to replace $P(\xi|x_1, \dots, x_N)$, and obtain

$$P(\xi|x_1, \dots, x_N) = \frac{P(\xi)P(x_1|\xi) \dots P(x_N|\xi)}{P(x_1)P(x_2|x_1) \dots P(x_N|x_1, \dots, x_{N-1})} \quad (64)$$

Replacing equation 64 in 63 yields

$$P(\xi) = \int_{\bar{x}} P(x_1)P(x_2|x_1) \dots P(x_N|x_1, \dots, x_{N-1}) \frac{P(\xi)P(x_1|\xi) \dots P(x_N|\xi)}{P(x_1)P(x_2|x_1) \dots P(x_N|x_1, \dots, x_{N-1})} d\bar{x} \quad (65)$$

Cancelling out all terms below the fraction bar (from equation 64) with the terms in front of the fraction bar (from equation 63) results in

$$P(\xi) = \int_{\bar{x}} P(\xi)P(x_1|\xi) \dots P(x_N|\xi) d\bar{x} \quad (66)$$

Using again *Bayes' Theorem* to replace all

$$P(x_v|\xi) = \frac{P(x_v)P(\xi|x_v)}{P(\xi)} \quad (67)$$

yields

$$P(\xi) = \frac{\int_{\bar{x}} P(\xi)P(x_1)P(\xi|x_1) \dots P(x_N)P(\xi|x_N) d\bar{x}}{P(\xi)^N} \quad (68)$$

$$P(\xi) = \frac{\int_{\bar{x}} P(x_1) \dots P(x_N)P(\xi|x_1) \dots P(\xi|x_N) d\bar{x}}{P(\xi)^{N-1}} \quad (69)$$

which is identical to equation 31. This proves that we can derive the final equation 38 without assuming independence of the observed distributions.

6. EXPRESSION IN CONVOLUTION ALGEBRA

In order to be able to efficiently compute equation 38 the integrals need to be expressed as convolutions, which can be computed in *Fourier Space* using the *Convolution Theorem*. Expressing equation 38 in convolution algebra (see also equation 3) requires two assumptions. Firstly, we assume the point spread functions $P(x_v|\xi)$ to be constant for every location in space. Secondly, we assume that the different coordinate systems ξ and $x_1 \dots x_N$ are identical, i.e. they are related by an identity transformation. We can assume that, as prior to the deconvolution the datasets have been aligned using the bead-based registration algorithm.¹⁴ The reformulation yields

$$\psi^{r+1} = \psi^r \prod_{v \in V} \frac{\phi_v}{\psi^r * P_v} * P_v^* \quad (70)$$

where $*$ refers to the convolution operator, \cdot and \prod to scalar multiplication, $-$ to scalar division and

$$P_v \equiv P(x_v|\xi) \quad (71)$$

$$\phi_v \equiv \phi_v(x_v) \quad (72)$$

$$\psi^r \equiv \psi^r(\xi) \quad (73)$$

Note that P_v^* refers to the mirrored version of kernel P_v (see section 2.1.1 for the explanation).

7. EFFICIENT BAYESIAN-BASED MULTI-VIEW DECONVOLUTION

Section 5 shows that the derivation of bayesian-based multi-view deconvolution does not require the assumption that the observed distributions (views) are independent. We want to take advantage of that and incorporate the relationship between them into the deconvolution process to reduce convergence time. In order to express these dependencies we need to understand and model the conditional probabilities $P(x_w|x_v)$ describing how one view $\phi_w(x_w)$ depends on another view $\phi_v(x_v)$.

7.1 MODELING CONDITIONAL PROBABILITIES

Let us assume that we made an observation $x_v = x'_v$ (see also supplementary figure 1b). The 'inverse' point spread function $Q(\xi|x_v)$ defines a probability for each location of the underlying distribution that it caused the event $\xi = \xi'$ that lead to this observation. Based on this probability distribution, the point spread function of any other observation $P(x_w|\xi)$ can be used to consecutively assign a probability to every of its locations defining how probable it is to expect an observation $x_w = x'_w$ corresponding to $x_v = x'_v$. Assuming the point spread function $P(x_w|\xi)$ is known, this illustrates that we are able to estimate the conditional probability $P(x_w|x_v = x'_v)$ for every location $x_w = x'_w$ as well as we can estimate the 'inverse' point spread function $Q(\xi|x_v)$.

However, we want to be able to compute an entire 'virtual' distribution, which is based on not only one singular event $x_v = x'_v$, but an entire observed distribution $\phi_v(x_v)$. Such a 'virtual' distribution is solely based on the conditional probabilities $P(x_w|x_v)$ and summarizes our knowledge about a distribution $\phi_w(x_w)$ by just observing $\phi_v(x_v)$ and knowing the (inverse) point spread functions $Q(\xi|x_v)$ and $P(x_w|\xi)$. We denote a 'virtual' distribution $\phi_v^{V_w}(x_w)$; the subscript v denotes the observed distribution it is based on, w defines the distribution that is estimated and V labels it as 'virtual' distribution.

The derivation of the formulation for a 'virtual' distribution is based on equations 3 and 10. The 'inverse' point spread function $Q(\xi|x_w)$ relates $\phi_v(x_v)$ to the underlying signal distribution $\psi(\xi)$, and the point spread function $P(x_w|\xi)$ consecutively relates it to the conditionally dependent signal distribution $\phi_w(x_w)$ (see also supplementary figure 1b)

$$\psi(\xi) = \int_{x_v} \phi_v(x_v) Q(\xi|x_v) dx_v \quad (74)$$

$$\phi_w(x_w) = \int_{\xi} \psi(\xi) P(x_w|\xi) d\xi \quad (75)$$

Substituting equation 74 in equation 75 yields

$$\phi_w(x_w) = \int_{\xi} \int_{x_v} \phi_v(x_v) Q(\xi|x_v) dx_v P(x_w|\xi) d\xi \quad (76)$$

As discussed in sections 2 and 3, we cannot use $Q(\xi|x_v)$ directly to compute $\psi(\xi)$. Using *Bayes' theorem* it can be rewritten as

$$Q(\xi|x_v) = \frac{\psi(\xi)P(x_v|\xi)}{\phi_v(x_v)} \quad (77)$$

Assuming $\phi_v(x_v)$ and $\psi(\xi)$ constant (or rather identical) simplifies equation 77 to

$$Q(\xi|x_v) = P(x_v|\xi) \quad (78)$$

This assumption reflects that initially we do not have any prior knowledge of $Q(\xi|x_v)$ and therefore need to set it equal to the PSF $P(x_v|\xi)$, which states the worst-case scenario. In other words, the PSF constitutes an *upper bound* for all possible locations of the underlying distribution $\psi(\xi)$ that could contribute to the observed distribution given an observation at a specific location $x_v = x'_v$. Thus, this assumption renders the estimate $\phi_v^{V_w}(x_w)$ less precise (equation 79 and main text figure 1c), while not omitting any of the possible solutions. Note that it would be possible to improve the guess of $Q(\xi|x_v)$ after every iteration. However, it would require a convolution with a different PSF at every location, which is currently computationally not feasible and is therefore omitted. Replacing equation 78 in equation 76 yields

$$\phi_w(x_w) \approx \phi_v^{V_w}(x_w) = \int_{\xi} \int_{x_v} \phi_v(x_v) P(x_v|\xi) dx_v P(x_w|\xi) d\xi \quad (79)$$

Equation 79 enables the estimation of entire 'virtual' distributions $\phi_v^{V_w}(x_w)$, see and main text figure 1c for a visualization. These 'virtual' distributions constitute an *upper boundary* describing how a distribution $\phi_w(x_w) \approx \phi_v^{V_w}(x_w)$ could look like while only knowing $\phi_v(x_v)$ and the two PSF's $P(x_v|\xi)$ and $P(x_w|\xi)$. We denote it *upper boundary* as it describes the combination of all possibilities of how a observed distribution $\phi_w(x_w)$ can look like.

7.2 INCORPORATING VIRTUAL VIEWS INTO THE DECONVOLUTION SCHEME

In order to incorporate this knowledge into the deconvolution process (equation 38), we perform updates not only based on the observed distributions $\phi_v(x_v)$ but also all possible virtual distributions $\phi_v^{V_w}(x_w)$ as modelled by equation 79 and shown in and main text figure 1c. Based on all observed distributions

$$V = \{\phi_1(x_1), \phi_2(x_2), \dots, \phi_N(x_N)\} \quad (80)$$

we can estimate the following 'virtual' distributions

$$W = \{\phi_1^{V_2}(x_2), \phi_1^{V_3}(x_3), \dots, \phi_1^{V_N}(x_N), \phi_2^{V_1}(x_1), \phi_2^{V_3}(x_3), \dots, \phi_2^{V_N}(x_N), \dots, \phi_N^{V_{N-1}}(x_{N-1})\} \quad (81)$$

where

$$|W| = (N - 1)^N : N = |V| \quad (82)$$

Note that if only one input view exists, $W = \emptyset$. We define subsets $W_v \subseteq W$, which depend on specific observed distributions $\phi_v(x_v)$ as follows

$$W_1 = \{\phi_1^{V_2}(x_2), \phi_1^{V_3}(x_3), \dots, \phi_1^{V_N}(x_N)\} \quad (83)$$

$$W_2 = \{\phi_2^{V_1}(x_1), \phi_2^{V_3}(x_3), \dots, \phi_2^{V_N}(x_N)\} \quad (84)$$

$$\dots \quad (85)$$

$$W_N = \{\phi_N^{V_1}(x_1), \phi_N^{V_2}(x_2), \dots, \phi_N^{V_{N-1}}(x_{N-1})\} \quad (86)$$

where

$$W = \bigcup_{v \in V} W_v \quad (87)$$

Incorporating the virtual distributions into the multi-view deconvolution (equation 38) yields

$$\psi^{r+1}(\xi) = \psi^r(\xi) \prod_{v \in V} \int_{x_v} \frac{\phi_v(x_v)}{\int_{\xi} \psi^r(\xi) P(x_v|\xi) d\xi} P(x_v|\xi) dx_v \prod_{w \in W_v} \int_{x_w} \frac{\phi_v^{V_w}(x_w)}{\int_{\xi} \psi^r(\xi) P(x_w|\xi) d\xi} P(x_w|\xi) dx_w \quad (88)$$

This formulation is simply a combination of observed and 'virtual' distributions, which does not yield any advantages in terms of computational complexity yet. During the following steps we will show that using a single assumption we are able to combine the update steps of the observed and 'virtual' distributions into one single update step for each observed distribution.

For simplicity we focus on one observed distribution $\phi_v(x_v)$ and its corresponding subset of 'virtual' distributions W_v . Note that the following assumptions and simplifications apply to all subsets individually.

$$\int_{x_v} \frac{\phi_v(x_v)}{\int_{\xi} \psi^r(\xi) P(x_v|\xi) d\xi} P(x_v|\xi) dx_v \prod_{w \in W_v} \int_{x_w} \frac{\phi_v^{V_w}(x_w)}{\int_{\xi} \psi^r(\xi) P(x_w|\xi) d\xi} P(x_w|\xi) dx_w \quad (89)$$

First, the 'virtual' distributions $\phi_v^{V_w}(x_w)$ are replaced with equation 79 which yields

$$\int_{x_v} \frac{\phi_v(x_v)}{\int_{\xi} \psi^r(\xi) P(x_v|\xi) d\xi} P(x_v|\xi) dx_v \prod_{w \in W_v} \int_{x_w} \frac{\int_{\xi} \int_{x_v} \phi_v(x_v) P(x_v|\xi) dx_v P(x_w|\xi) d\xi}{\int_{\xi} \psi^r(\xi) P(x_w|\xi) d\xi} P(x_w|\xi) dx_w \quad (90)$$

Note that $\int_{\xi} \psi^r(\xi) P(x_w|\xi) d\xi$ corresponds to our current guess of the observed distribution $\phi_w(x_w)$, which is based on the current guess of the underlying distribution $\psi^r(\xi)$ and the point spread function $P(x_w|\xi)$ (equation 3). In order to transform it into a 'virtually' observed distribution compatible with $\phi_v^{V_w}(x_w)$, we also apply equation 79, i.e. we compute it from the current guess of the observed distribution $\phi_v(x_v)$ yielding

$$\int_{x_v} \frac{\phi_v(x_v)}{\int_{\xi} \psi^r(\xi) P(x_v|\xi) d\xi} P(x_v|\xi) dx_v \prod_{w \in W_v} \int_{x_w} \frac{\int_{\xi} \int_{x_v} \phi_v(x_v) P(x_v|\xi) dx_v P(x_w|\xi) d\xi}{\int_{\xi} \int_{x_v} \int_{\xi} \psi^r(\xi) P(x_v|\xi) d\xi P(x_v|\xi) dx_v P(x_w|\xi) d\xi} P(x_w|\xi) dx_w \quad (91)$$

To better illustrate the final simplifications we transform equation 91 into convolution algebra (section 6). The reformulation yields

$$\frac{\phi_v}{\psi^r * P_v} * P_v^* \prod_{w \in W_v} \frac{\phi_v * \overbrace{P_v^* * P_w}^{\text{bracket}}}{\psi^r * P_v * \underbrace{P_v^* * P_w}_{\text{bracket}}} * P_w^* \quad (92)$$

Additional simplification of equation 92 requires an assumption in convolution algebra that we incorporate twice. Given three functions f , g and h we assume

$$(f * g) \cdot (f * h) \approx f * (g \cdot h) \quad (93)$$

We illustrate in supplementary figure 3 on a one-dimensional and two-dimensional example that for *Gaussian*-like distributions this assumption may hold true after normalization of both sides of the equation. Note that the measured PSF's usually resemble a distribution similar to a gaussian (supplementary figure 5 and 10).

The numerator and the denominator of the ratio of the 'virtual' distribution in equation 92 both contain two consecutive convolutions with P_v^* and P_w as indicated by brackets. Based on equation 93 we assume

$$\frac{(g * f)}{(h * f)} \approx \left(\frac{g}{h}\right) * f \quad (94)$$

where

$$f \equiv P_v^* * P_w \quad (95)$$

$$g \equiv \phi_v \quad (96)$$

$$h \equiv \psi^r * P_v \quad (97)$$

and

$$\frac{(g * f)}{(h * f)} = (g * f) \cdot \frac{1}{(h * f)} = (g * f) \cdot \left(\frac{1}{h} * f \right) = \overbrace{(f * g) \cdot \left(f * \frac{1}{h} \right)}^{\text{equation 93}} \approx f * \left(g \cdot \frac{1}{h} \right) = f * \left(\frac{g}{h} \right) = \left(\frac{g}{h} \right) * f \quad (98)$$

Based on this assumption we can rewrite equation 92 as

$$\overbrace{\frac{\phi_v}{\psi^r * P_v} * P_v^*} \prod_{w \in W_v} \overbrace{\frac{\phi_v}{\psi^r * P_v} * P_v^* * P_w * P_w^*} \quad (99)$$

Note that this reformulation yields two identical terms as outlined by brackets describing the ratio between the observed distribution ϕ_v and its guess based on the current iteration of the deconvolved distribution $\psi^r * P_v$. To further simplify equation 99 we apply the assumption (equation 93) again where

$$f \equiv \frac{\phi_v}{\psi^r * P_v} \quad (100)$$

$$g \equiv P_v^* \quad (101)$$

$$h \equiv P_v^* * P_w * P_w^* \quad (102)$$

which yields

$$\frac{\phi_v}{\psi^r * P_v} * \left(P_v^* \prod_{w \in W_v} P_v^* * P_w * P_w^* \right) \quad (103)$$

In the context of all observed distributions, the final formula for efficient bayesian-based multi-view deconvolution reads

$$\psi^{r+1} = \psi^r \prod_{v \in V} \frac{\phi_v}{\psi^r * P_v} * \overbrace{\left(P_v^* \prod_{w \in W_v} P_v^* * P_w * P_w^* \right)}^{P_v^{\text{compound}}} \quad (104)$$

Equation 104 incorporates all observed and 'virtual' distributions that speed up convergence, but requires the exactly same number of computations as the normal multi-view deconvolution (equation 38) derived in section 3. The only additional computational overhead is the initial computation of the *compound* kernels for each observed distribution

$$P_v^{\text{compound}} = P_v^* \prod_{w \in W_v} \overbrace{P_v^* * P_w * P_w^*}^{P_{w_v}^{\text{compound}}} \quad (105)$$

The compound kernel for a specific observed distribution ϕ_v is computed by scalar multiplication of its mirrored point spread function P_v^* with all 'virtual' compound kernels $P_{w_v}^{\text{compound}}$ based on the corresponding 'virtual' distributions $\phi_v^{V,w}(x_w) \in W_v$. All individual 'virtual' compound kernels are computed by convolving P_v^* with P_w and sequentially with P_w^* . For most multi-view deconvolution scenarios the computational effort for the pre-computation of the compound kernels can be neglected as the PSF's are very small compared to the images and they need to be computed only once.

8. AD-HOC OPTIMIZATIONS OF THE EFFICIENT BAYESIAN-BASED MULTI-VIEW DECONVOLUTION

The efficient bayesian-based multi-view deconvolution derived in section 7 offers possibilities for optimizations as the assumption underlying the estimation of the conditional probabilities (section 7.1) results in smoothed guess of the 'virtual' distributions (and main text figure 1c). Therefore, the core idea underlying all subsequently presented alterations of equation 104 is to change how the 'virtual' distributions are computed. Due to the optimizations introduced in the last section, this translates to modification of the 'virtual' compound kernels

$$P_{w_v}^{compound} = P_v^* * P_w * P_w^* \quad (106)$$

The goal is to decrease convergence time while preserving reasonable deconvolution results. This can be achieved by sharpening the 'virtual' distribution (and main text figure 1c) without omitting possible solutions or rendering them too unlikely.

8.1 OPTIMIZATION I - REDUCED DEPENDENCE ON VIRTUALIZED VIEW

The computation of the 'virtual' compound kernels contains two convolutions with the point spread function of the 'virtualized' observation, one with P_w and one with P_w^* . We found that skipping the convolution with P_w^* significantly reduces convergence time while producing almost identical results even in the presence of noise (section 10 and 10.5).

$$\psi^{r+1} = \psi^r \prod_{v \in V} \frac{\phi_v}{\psi^r * P_v} * \left(P_v^* \prod_{w \in W_v} P_v^* * P_w \right) \quad (107)$$

8.2 OPTIMIZATION II - NO DEPENDENCE ON VIRTUALIZED VIEW

We determined empirically that further assuming P_w to be constant still produces reasonable results while further reducing convergence time. We are aware that this is quite an ad-hoc assumption, but in the presence of low noise levels still yields adequate results (section 10 and 10.5).

$$\psi^{r+1} = \psi^r \prod_{v \in V} \frac{\phi_v}{\psi^r * P_v} * \prod_{v, w \in W_v} P_v^* \quad (108)$$

Interestingly, this formulation shows some similarity to an optimization of the classic single-view Richardson-Lucy deconvolution, which incorporates an exponent into the entire 'correction factor',²⁴ not only the PSF for the second convolution operation. Our derivation of the efficient bayesian-based multi-view scenario intrinsically provides the exponent for the second convolution that can be used to speed up computation and achieve reasonable results.

8.3 NO DEPENDENCE ON OBSERVED VIEW

Only keeping the convolutions of the 'virtualized' observation, i.e. P_w and P_w^* yields a non-functional formulation. This is in agreement with the estimation of the conditional probabilities (section 7.1).

9. ALTERNATIVE ITERATION FOR FASTER CONVERGENCE

To further optimize convergence time we investigated the equations 38 and 104 in detail. Both multi-view deconvolution formulas evaluate all views in order to compute one single update step of $\psi(\xi)$. It was already noted that in both cases each update step is simply the **multiplication** of all contributions from each observed distribution. This directly suggests an alternative update scheme where the individual contributions from each

observed distribution are directly multiplied to update $\psi(\xi)$ in order to save computation time. In this iteration scheme, equation 104 reads as follows

$$\psi^{r+1} = \psi^r \frac{\phi_1}{\psi^r * P_1} * \left(P_1^* \prod_{w \in W_1} P_1^* * P_w * P_w^* \right) \quad (109)$$

$$\psi^{r+2} = \psi^{r+1} \frac{\phi_2}{\psi^{r+1} * P_2} * \left(P_2^* \prod_{w \in W_2} P_2^* * P_w * P_w^* \right) \quad (110)$$

$$\dots \quad (111)$$

$$\psi^{r+N} = \psi^{r+N-1} \frac{\phi_N}{\psi^{r+N-1} * P_N} * \left(P_N^* \prod_{w \in W_N} P_N^* * P_w * P_w^* \right) \quad (112)$$

$$(113)$$

Note that for equation 38 (equation 70) the iterative scheme looks identical when the multiplicative part of the compound kernel is left out; it actually corresponds to the sequential application of the standard Richardson-Lucy (RL) updates (equation 13), which corresponds to the principle of *Ordered Subset Expectation Maximization*⁶ (OS-EM, see section 9.1).

9.1 RELATIONSHIP TO ORDERED SUBSET EXPECTATION MAXIMIZATION (OS-EM)

The principle of OS-EM is the sequential application of *subsets* of the observed data to the underlying distribution $\psi(\xi)$ using standard Richardson-Lucy (RL) updates (equation 13). Note that in a multi-view deconvolution scenario, each observed distribution $\phi_v(x_v)$ is equivalent to the OS-EM definition of a *balanced subset* as all elements of the underlying distribution are updated for each $\phi_v(x_v)$.

$$\psi^{r+1}(\xi) = \psi^r(\xi) \int_{x_1} \frac{\phi_1(x_1)}{\int_{\xi} \psi^r(\xi) P(x_1|\xi) d\xi} P(x_1|\xi) dx_1 \quad (114)$$

$$\psi^{r+2}(\xi) = \psi^{r+1}(\xi) \int_{x_2} \frac{\phi_2(x_2)}{\int_{\xi} \psi^{r+1}(\xi) P(x_2|\xi) d\xi} P(x_2|\xi) dx_2 \quad (115)$$

$$\dots \quad (116)$$

$$\psi^{r+N}(\xi) = \psi^{r+N-1}(\xi) \int_{x_N} \frac{\phi_N(x_N)}{\int_{\xi} \psi^{r+N-1}(\xi) P(x_N|\xi) d\xi} P(x_N|\xi) dx_N \quad (117)$$

As pointed out in the main text, the obvious relationship to OS-EM is that the sequential application of RL updates is directly suggested by our multiplicative derivation (equation 38), compared to the additive EM derivation.⁵

10. BENCHMARKS

We compare the performance of our new derivations against classical multi-view deconvolution (section 10.1) and against other optimized multi-view deconvolution schemes (section 10.2) using ground truth images. Subsequently, we investigate the general image quality (section 10.3), the dependence on the PSF's (section 10.4), analyze the effect of noise and regularization (section 10.5) and show the result of imperfect point spread functions (section 10.6).

The iteration behaviour of the deconvolution depends on the image content and the shape of the PSF (supplementary figure 4d). In order to make the simulations relatively realistic for microscopic multi-view acquisitions, we chose as ground truth image one plane of a SPIM acquisition of a *Drosophila* embryo expressing His-YFP in all cells (supplementary figure 5a,e) that we blur with a maximum intensity projection of a PSF in axial direction (xz), extracted from an actual SPIM acquisition (supplementary figure 5e).

10.1 CONVERGENCE TIME, NUMBER OF ITERATIONS & UPDATES COMPARED TO CLASSICAL MULTI-VIEW DECONVOLUTION

First, we compare the performance of the efficient bayesian-based multi-view deconvolution (section 7, equation 104) and its optimizations I & II (sections 8.1 and 8.2, equations 107 and 108) against the Bayesian-based derivation (sections 3 and 5, equations 38 and 70) and the original Maximum-Likelihood Expectation-Maximization derivation⁵ for combined (sections 3 – 8) and sequential (section 9, OSEM⁶) updates of the underlying distribution.

Supplementary figure 4a-c illustrate computation time, number of iterations and number of updates of the underlying distribution that are required by the different derivations to converge to a point, where they achieve exactly the same average difference between the deconvolved image and the ground truth. Detailed parts of the ground truth, PSFs, input images and results used for supplementary figure 4 are exemplarily pictured for 4 views in supplementary figure 5e, illustrating that all algorithms actually converge to the same result. The entire ground truth picture is shown in supplementary figure 5a, the deconvolution result as achieved in the benchmarks is shown in supplementary figure 5b.

Supplementary figure 4a shows that our efficient Bayesian-based deconvolution (equation 104) outperforms the Bayesian-based deconvolution (equation 38) by a factor of around 1.5–2.5, depending on the number of views involved. Optimization I is faster by a factor of 2–4, optimization II by a factor of 3–8. Sequential updates (OSEM) pictured in red additionally speed up the computation by a factor of approximately n , where n describes the number of views involved. This additional multiplicative speed-up is independent of the derivation used. Supplementary figure 4b illustrates that our Bayesian-based deconvolution behaves very similar to the Maximum-Likelihood Expectation-Maximization method.⁵ Note the logarithmic scale of all y-axes in supplementary figure 4.

It is striking that for combined updates (black) the computation time first decreases, but quickly starts to increase with the number of views involved. In contrast, for sequential updates (OSEM) the computation time decreases and then plateaus. The increase in computation time becomes clear when investigating the required number of iterations^{††} (supplementary figure 4b). The number of iteration for combined updates (black) almost plateaus at a certain level, however, with increasing number of views, the computational effort to compute one update increases linearly. This leads to an almost linear increase in convergence time with an increasing number of views when using combined updates. When using sequential updates (red), the underlying distribution is updated for each view individually, hence the number of required iterations continuously decreases and only the convergence time plateaus with an increasing number of views. Supplementary figure 4c supports this interpretation by illustrating that for each derivation the number of updates of the underlying distribution defines when the same quality of deconvolution is achieved.

In any case, having more than one view available for the deconvolution process decreases computation time and number of required updates significantly. This effect is especially prominent at a low number of views. For example adding a second view decreases the computation time in average 45-fold, a third view still on average another 1.5-fold.

One can argue that using combined update steps allows better parallelization of the code as all view contributions can be computed at the same time, whereas sequential updating requires to compute one view after the other. In practice, computing the update step for an individual view is already almost perfectly multi-threadable. It requires two convolutions computed in Fourier space and several per-pixel operations. Even when several GPU's are available it can be parallelized as it can be split into blocks. Using sequential updates additionally offers the advantage that the memory required for the computation is significantly reduced.

^{††}Note that we consider one iteration completed when all views contributed to update the underlying distribution once. In the case of combined updates this refers to one update of the underlying distribution, in case of sequential updates this refers to n updates.

10.2 CONVERGENCE TIME, NUMBER OF ITERATIONS & UPDATES COMPARED TO OTHER OPTIMIZED MULTI-VIEW DECONVOLUTION SCHEMES

Previously, other efficient methods for optimized multi-view deconvolution have been proposed. We compare our methods against Scaled-Gradient-Projection (SGP),⁸ Ordered Subset Expectation Maximization (OSEM)⁶ and Maximum a posteriori with Gaussian Noise (MAPG).⁷ Again, we let the algorithms converge until they achieve the same average difference of 0.07 to the known ground truth image.

In order to compare the different algorithms we re-implemented MAPG in Java, based on the Python source code kindly provided by Dr. Peter Verveer. In order to compare to SGP, we downloaded the IDL source code. In order to allow a reasonable convergence, it was necessary to add a constant background to the images before processing them with SGP. It was also necessary to change the size of the input data to a square, even dimension (614×614) to not introduce a shift of one pixel in the deconvolved data by the IDL code. OSEM is identical to our sequential updates and therefore requires no additional implementation. Main text figure 1f illustrates that our Java implementation (Bayesian-based + OSEM) and the IDL OSEM implementation require almost the identical amount of iterations.

Regarding the number of iterations (main text figure 1f), the efficient Bayesian-based deconvolution and Optimization I perform better compared to all other efficient methods for more than 4 overlapping views, Optimization II already for more than 2 views. For example at 7 views, where OSEM (50), SGP (53) and MAPG (44) need around 50 iterations, the efficient Bayesian-based deconvolution requires 23 iteration, Optimization I 17 iterations, and Optimization II 7 iteration in order to converge to the same result.

Concerning computation time (main text figure 1e), any algorithm we implemented in Java completely outperforms any IDL implementation. For the almost identical implementation of OSEM Java is in average 8× faster than IDL on the same machine (2× Intel Xeon E5-2680, 128 GB RAM), which slightly increases with the number of views (7.89× for 2 views, 8.7× for 11 views). Practically, Optimization II outperforms all methods, except MAPG at 2 views. At 7 views where SGP (IDL) and OSEM (IDL) require around 80 seconds to converge, MAPG converges in 4 seconds, the efficient Bayesian-based deconvolution in 5 seconds, Optimization I in 3.7 seconds and Optimization II in 1.6 seconds.

Note that MAPG is conceptually different to all other deconvolution methods compared here. It assumes Gaussian noise and performs the deconvolution on a fused dataset, which results in a reduced reconstruction quality on real datasets (see also section 10.3.1). It also means that its computation time is theoretically independent on the number of views, a property that is shared with the classical OSEM (Supplementary figure 4c). However, it is obvious that up to 4 views, the deconvolution performance significantly increases with an increasing number of views. We speculate that the reason for this is the coverage of frequencies in the Fourier spectrum. Each PSF view blurs the image in a certain direction, which means that certain frequencies are more preserved than others. For more than 4 views, it seems that most high frequencies are contributed by at least one of the views and therefore the performance does not increase any more for algorithms that do not take into account the relationships between the individual views. Note, that our optimized multi-view deconvolution methods still significantly increase their performance if more than 4 views contribute (main text figure 1d,e and supplementary figure 4a,b,c).

Supplementary figure 6a plots the computation time versus the image size of the deconvolved image for a dataset consisting of 5 views. All methods behave more or less proportional, however, the IDL code is only able to process relatively small images.

Supplementary figure 6b illustrates that our optimizations can theoretically also be combined with SGP, not only OSEM. The number of iterations is in average reduced 1.4-fold for the efficient Bayesian-based deconvolution, 2.5-fold for Optimization I, and 2.5-fold for Optimization II.

10.3 VISUAL IMAGE QUALITY

Supplementary figure 5c shows the result using optimization II and sequential updates (OSEM) after 14 iterations, the same quality as achieved by all algorithms as shown in supplementary figure 5e and used for the

benchmarks in supplementary figure 4. In this case the quality of the deconvolved image is sufficient to separate small details like the fluorescent beads, which is not possible in the input images (supplementary figure 5e, right top). 301 iterations almost perfectly restore the image (supplementary figure 5b,d). In comparison, the Bayesian-based derivation (equation 38) needs 301 iteration to simply arrive at the quality pictured in supplementary figure 5c,e.

10.3.1 COMPARISON TO MAPG

Supplementary figure 6c-h compares our fastest Optimization II to MAPG using the same 7-view acquisition of a *Drosophila* embryo expressing His-YFP as in main text figure 3c-e. It shows that, despite being significantly faster than MAPG (main text figure 1e,f), Optimization II clearly outperforms MAPG in terms of overall image quality (supplementary figure 6c-h). Using the same blending scheme (supplementary figure 17) MAPG produces artifacts close to some of the nuclei (e.g. top left of supplementary figure 6e) and enhances stripes inside the sample that arise from the beginning/ending of partially overlapping input views. Especially the lower part of supplementary figure 6c shows reduced quality, which most likely arises from the fact that in that area one input view less contributes to the final deconvolved image (note that the 7 views are equally spaced in 45 degree steps from 0–270 degrees, however every pixel is covered by at least 2 views). Note that also Optimization II shows slightly reduced image quality in this area, but is able to compensate the reduced information content significantly better.

10.4 GENERAL DEPENDENCE ON THE PSF's

For supplementary figure 4a-c the PSF's are arranged in a way so that the angular difference between them is maximal in the range from 0–180 degrees (supplementary figure 5e). Supplementary figure 4d visualizes for 4 views that the angular difference between the views significantly influences the convergence behaviour. Looking at two extreme cases explains this behaviour. In this synthetic environment a difference of 0 degrees between PSF's corresponds to 4 identical PSF's and therefore 4 identical input images. This constellation is identical to having just one view, which results in a very long convergence time (supplementary figure 4a). The same almost applies for 180 degrees as the PSF that was used is quite symmetrical. In those extreme cases our argument that we can learn something about a second view by looking at the first view (section 7.1) does not hold. Therefore our efficient Bayesian-based deconvolution as well as the optimizations do not converge to the identical result and few datapoints close and equal to 0 and 180 degrees are omitted. Note that they still achieve a reasonable result, but simply cannot be plotted as this quality of reconstruction is not achieved.

In general, convergence time decreases as the level of overlap between the PSFs decreases. In case of non-isotropic, gaussian-like PSFs rotated around the center (as in multi-view microscopy), this translates to a decrease in convergence time with an increase in angular difference. From this we can derive that for overlapping multi-view acquisitions it should be advantageous to prefer an odd over an even number of equally spaced views.

Supplementary figure 4d also illustrates that convergence time significantly depends on the shape and size of the PSF. Different PSF's require different amount of iterations until they reach the same quality. Intuitively this has to be true, as for example the most simple PSF consisting only of its central pixel does not require any deconvolution at all. Conversely, this also holds true for the images themselves; the iteration time required to reach a certain quality depends on the content. For example, the synthetic image used in Supplementary Movie 1 takes orders of magnitude longer to converge to same cross correlation of 0.99 to ground truth, compared to the image in supplementary figure 5a using the same PSF's, algorithm and iteration scheme.

10.5 NOISE AND REGULARIZATION

Although the signal-to-noise ratio is typically very high in light-sheet microscopy (see Supplementary Table 1), it is a common problem and we therefore investigated the effect of noise on the performance of the different

algorithms. As Poisson noise is the dominant source of noise in light microscopy we created our simulated input views using a Poisson process with variable SNR:

$$SNR = \sqrt{N} \quad (118)$$

where N is the number of photons collected. These images were then used to run the deconvolution process. The first row in supplementary figure 7a and first column in supplementary figure 8 show the resulting input data for varying noise levels. For supplementary figure 8c we added Gaussian noise with an increasing mean to simulate the effects of Gaussian noise.

A comparison as in the previous section is unfortunately not possible as in the presence of noise none of the algorithms converges exactly towards the ground truth. Note that still very reasonable results are achieved as shown in supplementary figure 7a and 8. Therefore, we devised a different scenario to test the robustness to noise. For the case of no noise ($SNR = \infty$) we first identified the number of iterations required for each algorithm to reach the same quality (supplementary figure 7c, 1st column). With increasing noise level we iterate the exact same number of iterations for each algorithm and analyze the output.

Supplementary figure 7a,b,c show that for the typical regime of SNR's in light sheet microscopy (see Supplementary Table 1, estimation range from 15 to 63) all methods converge to visually identical results.

For low SNR's (independent of Poisson or Gaussian noise) the Bayesian-based deconvolution (equation 38), the Maximum-Likelihood Expectation-Maximization (ML-EM) and the sequential updates (OSEM) score best with almost identical results. For Poisson noise, MAPG and Optimization II show comparable results with lower quality, Optimization I and the efficient Bayesian-based derivation lie in between. For Gaussian noise, MAPG, the Bayesian-based derivation and Optimization I produce very similar results while Optimization II shows lower quality.

To compensate for noise in the deconvolution we added the option of Tikhonov-regularization. Supplementary figure 7c illustrates the influence of the λ parameter on the deconvolution results. Supplementary figure 8 shows corresponding images for all data points. We think that although the Tikhonov regularization slows down convergence (supplementary figure 7c), a low λ might be a good choice even in environments of a high SNR (supplementary figure 8).

10.6 PSF-ESTIMATION

Another common source of errors is an imprecise estimation of the PSF's. In the previous sections we always assumed to know the PSF exactly. In real life PSF's are either measured or theoretically computed and might therefore not precisely resemble the correct system PSF of the microscope due to misalignment, refractions, etc.

In order to be able to estimate the effect of using imprecise PSF's for the deconvolution we randomly rotated the PSF's we used to create the input images before applying them to the deconvolution (supplementary figure 9). We used the same scheme to analyze the results as discussed in section 10.5. Surprisingly, the effect on the deconvolution result is hardly noticeable for all algorithms, even at an average rotation angle of 10 degrees. The deconvolved images are practically identical (therefore not shown), the maximal difference in the correlation coefficient is $r=0.017$. We suspect that this is a result of the almost Gaussian shape of the PSF's. Although the correct solution becomes less probable, it is still well within range.

We investigated the change of the PSF of a SPIM system that should occur due to concavity of the light sheet across the field of view. Typical light-sheet microscopic acquisitions as shown in supplementary figure 10 and 16 show no visible sign of change, even across the entire field of view. Given the tolerance of the deconvolution regarding the shape of the PSF we concluded that it is not necessary to extract different PSFs at different physical locations. Note that the option to perform the deconvolution in blocks (section 14.1) would easily allow such an extension. We think that another real improvement in deconvolution quality could be achieved by being able to measure the correct PSF inside the sample, which could be combined with the work from Blume et al.²⁵ Additionally to the experimental burden, it is unfortunately far from being computationally tractable.

11. MULTI-VIEW DECONVOLUTION, RESOLUTION AND OTHER OPTICAL SECTIONING MICROSCOPY

In order to better characterize the gain of multi-view deconvolution we performed several experiments and comparisons. In supplementary figure 12 we compare a multi-view acquisition done with SPIM to a single-view acquisition done by two-photon microscopy of the same sample. The fixed *Drosophila* embryo stained with Sytox green was embedded into agarose and first imaged using a $20\times/0.5\text{NA}$ water dipping objective in the Zeiss SPIM prototype. After acquisition we cut the agarose and imaged the same sample with a two-photon microscope using a $20\times/0.8\text{NA}$ air objective. The datasets could be aligned using the fluorescent beads present in the SPIM and two-photon acquisition. Supplementary figure 12 compares the quality of the content-based multi-view fusion and multi-view deconvolution of the SPIM dataset to the two-photon stack and a Lucy-Richardson single-view deconvolution of the two-photon stack. While two-photon microscopy is able to detect more photons in the center of the embryo (supplementary figure 12c), the multi-view deconvolution shows significantly better resolution and coverage of the sample.

Supplementary figure 13 illustrates that a multi-view deconvolution can principally be done by any optical sectioning microscope that is capable of sample rotation. We acquired a multi-view dataset using Spinning Disc Confocal microscopy and a self-built rotational device.¹⁴ We compare the quality of one individual input stack with the multi-view deconvolution and the single-view deconvolution of this stack. Although one view completely covers the sample, it is obvious that the multi-view deconvolution clearly improves the resolution compared to the single-view deconvolution (most obvious in supplementary figure 13d, please zoom in to investigate details).

Supplementary figure 11 visually compares raw light-sheet data, the result of content-based multi-view fusion and the multi-view deconvolution with Structured Illumination of DSLM data (SIM).¹⁶ It is obvious that SIM and multi-view deconvolution significantly increase contrast. We are, however, not able from the published data alone to make any statement on the increase of resolution by SIM compared to multi-view deconvolution.

To be able to quantify the gain in resolution we focused our analysis on the fluorescent beads (supplementary figure 14). We extracted all corresponding fluorescent beads from two input views, after multi-view fusion and after multi-view deconvolution. Comparing the input views and the multi-view fusion, it becomes apparent that the multi-view fusion reduces resolution in all dimensions except directly in the axial resolution of the input view. The multi-view deconvolution on the other hand increases resolution in all dimensions compared to the multi-view fused data. The multi-view deconvolution actually achieves almost isotropic resolution in all dimensions at least comparable to the resolution of each input stack in lateral direction.

12. PARTIALLY OVERLAPPING DATASETS

In practical multi-view deconvolution scenarios where large samples are acquired on light-sheet microscopes, it is often the case that not all views are entirely overlapping (e.g. main text figure 3c,d,e and supplementary figure 11, 15, and 16). The sequential update strategy (OSEM) intrinsically supports partially overlapping datasets as it allows to only update parts of the underlying distribution using subsets of the input data. It is, however, necessary to achieve a balanced update of all pixels of the underlying distribution (supplementary figure 17a,b). To achieve that, we initially compute a weight image for each view. It consists of a blending function returning 1 in all central parts of a view; close to the boundaries weights are decreasing from 1 and 0 following a cosine function.¹⁴ This avoids artifacts due to hard edges arising from partial overlap (supplementary figure 17a).

It is important to note that for the normalizations individual weights are never increased above 1. It would otherwise lead to bigger steps than suggested by one Lucy-Richardson update step making the gradient descent of the deconvolution unstable.

On each sequential update step the weight (0...1) of each pixel of every view defines the fraction of change suggested by a Lucy-Richardson update step that will be applied to the deconvolved image. By default, the sum of weights of each individual pixel in the deconvolved image over all input view is normalized to ≤ 1 (supplementary figure 17b-l). This provides the most uniform update of the deconvolved image possible.

It is, however, identical to not using OSEM in terms of performance (supplementary figure 17d left) and provides no improvement over the Bayesian-based derivation. Note that it still reduces the memory requirements significantly.

In order to benefit from the OSEM speedup, it is necessary to find a reasonable number of overlapping views per pixel for a specific acquisition. It is not suggested to update every pixel with the full available weights of all input views as it leads to an uneven deconvolution, i.e. some areas will be sharper than others. We found that in most cases the minimal number of overlapping views (supplementary figure 17b–II, c) will provide a reasonable tradeoff between speed-up and uniformity. Some areas close to the boundaries of the input views might still be less deconvolved, but only if those areas are close to the boundary of one of the input views.

In summary, the speedup achieved in partly overlapping datasets is the same as in completely overlapping datasets. However, less views overlap, which increases convergence time. Our optimizations increase the performance in any case (supplementary figure 17d).

In order to let the user make a reasonable choice of the number of overlapping datasets we offer the safe choice of 1, the minimal number of views, the average number of views, or a user-defined value. The Fiji plugin also offers the option to output an image that shows the number of contributing view at every pixel in the deconvolved image. This offers the chance to select a reasonable value or maybe give hints in how to adjust the imaging strategy (number of views, size of stacks, etc.). Please note that also in real data, datasets are often completely overlapping (e.g. main text figure 3a,b,e,f,g and supplementary figure 13).

13. SIMULATION OF SPIM DATA

We simulate a three dimensional (3d) ground truth dataset that resembles a biological object such as an embryo or a spheroid (main text figure 2a, section 13.1). The simulated multi-view microscope rotates the sample around the x-axis, attenuates the signal, convolves the input, samples at lower axial resolution, and creates the final sampled intensities using a poisson process. A link to the *Java source code* for the simulation and 3d volume rendering can be found in section 14.2.

In order to simulate a specific input view for the multi-view deconvolution, we first rotate the ground truth image around the x-axis by n° (section 13.2). This corresponds to the orientation in which the virtual microscope performs an acquisition. Secondly, we perform the acquisition by applying all degradations as outlined above (main text figure 2b, sections 13.3–13.5). Finally, we rotate the acquired 3d image back into the orientation of the ground truth image (section 13.6). This corresponds to the task of multi-view registration in real multi-view datasets. Two examples of input views are pictured in main text figure 2c.

13.1 BIOLOGICAL OBJECT SIMULATION

We use `ImgLib2`¹⁹ to draw a 3d sphere consisting of many small 3d spheres that have random locations, size and intensity. We simulate at twice the resolution of the final ground truth image and downsample the result to avoid too artificial edges.

13.2 INITIAL TRANSFORMATION

The initial rotation around the x-axis orients the ground truth image so that the virtual microscope can perform an acquisition. However, every transformation of an image introduces artifacts due to interpolation. While on a real microscope this initial transformation is performed physically and thus obviously does not introduce any artifacts, this initial transform is required for the simulation. To avoid that those artifacts are only present in the simulated views and not in the ground truth image (which might interfere with results), we also rotate the ground truth image by 15° around the rotation axis of the simulated multi-view microscope, i.e. all simulated input views are rotated by $(n + 15)^\circ$ around the x-axis. The resulting ground truth image is depicted in main text figure 2a.

13.3 SIGNAL ATTENUATION

We simulate the signal degradation along the lightsheet using a simple physical model of light attenuation.²⁶ Based on an initial amount of laser power (or number of photons), the sample will absorb a certain percentage of photons at each spatial location, depending on the absorption rate ($\delta = 0.01$) and the probability density (intensity) of the ground truth image. An example of the resulting image is shown in main text figure 2b.

13.4 CONVOLUTION

To simulate excitation and emission PSF as well as light sheet thickness, we measured effective PSF's from fluorescent beads of real multi-view dataset taken with the Zeiss SPIM prototype and a 40x/0.8NA water dipping objective. We convolve the attenuated image with different PSF's for each view. An example of the resulting image is shown in main text figure 2b.

13.5 SAMPLING AND NOISE

To simulate the reduced axial resolution we sample only every third slice in axial (z) direction, but every pixel in lateral direction (xy). This corresponds to a typical multi-view acquisition (Supplementary Table 1). The sampling process for each pixel is a poisson process, with the intensity of the convolved pixel being its average. An example of the resulting image is shown in main text figure 2b.

13.6 MULTI-VIEW REGISTRATION

To align all simulated views, we first scale them to an isotropic volume and then rotate them back into the original orientation of the ground truth data. Linear interpolation is used for all transformations.

13.7 REMARKS ON RESULTS

Main text figure 2e,f shows that MAPG and Optimization II outperform content-based fusion in terms of spatial resolution. However, MAPG shows strong ring-like artifacts at the outlines of the simulated spheres. Supplementary movie 3 shows additional artificial patterns produced by MAPG. Computation time is measured until the maximal cross correlation to the ground truth is achieved. Note that manual stopping of the deconvolution at earlier stages can reduce noise in the deconvolved image.

14. IMPLEMENTATION DETAILS

14.1 DECONVOLUTION

The multi-view deconvolution is implemented in Fiji¹⁸ using ImgLib.¹⁹ Performance critical tasks are the convolutions with the PSF's or the compound kernels. We implement them using Fourier convolutions and provide an alternative implementation of the Fourier convolution on the GPU. Note that it is not possible to implement the entire pipeline on the GPU due to the limited size of graphics card memory. All significant parts of implementation including per-pixel operations, copy and paste of blocks and the Fast Fourier Transform are completely multi-threaded to allow maximal execution performance on the CPU and GPU. The source code is available on Github: <https://github.com/fiji/spimreconstruction>. The source code most relevant to the deconvolution can be found in the package `src.main.java.mpicbg.spim.postprocessing.deconvolution2`.

14.2 SIMULATION AND RENDERING

The simulation of multi-view data (section 13) and the 3d-rendering as shown in main text figure 2a are implemented in ImgLib2.¹⁹ The source code for the simulation is available on Github: <https://github.com/StephanPreibisch/multiview-simulation>. The source code for the 3d volume rendering can be found on Github as well <https://github.com/StephanPreibisch/volume-renderer>. Please note that this is a fork of the volume renderer written by Stephan Saalfeld <https://github.com/axtimwalde/volume-renderer>, the relevant class for rendering the sphere is `net.imglib2.render.volume.RenderNatureMethodsPaper.java`

14.3 FIJI-PLUGIN

The multi-view deconvolution is integrated into Fiji (<http://fiji.sc>), please make sure to update Fiji before you run the multi-view deconvolution. The typical workflow consists of three steps.

1. The first step is to run the bead-based registration¹⁴ on the data (http://fiji.sc/SPIM_Bead_Registration, [Fiji – Plugins – SPIM Registration – Bead-based registration](#)).
2. The second step is to perform a simple average multi-view fusion in order to define the correct bounding box on which the deconvolution should be performed (http://fiji.sc/Multi-View_Fusion, [Fiji – Plugins – SPIM Registration – Multi-view fusion](#)).
3. The final step is to run the multi-view deconvolution using either the GPU or the CPU implementation (http://fiji.sc/Multi-View_Deconvolution, [Fiji – Plugins – SPIM Registration – Multi-view deconvolution](#)).

Detailed instructions on how to run the individual plugins can be found on their respective Fiji wiki pages, they are summarized on this page http://fiji.sc/SPIM_Registration. Note that due to the scripting capabilities of Fiji, the workflow can be automated and also for example be executed on a cluster (http://fiji.sc/SPIM_Registration_on_cluster).

Note: An example dataset is available for download on the Fiji page: http://fiji.sc/SPIM_Registration#Downloading_example_dataset.

14.4 GPU IMPLEMENTATION

The GPU implementation based on CUDA (http://www.nvidia.com/object/cuda_home_new.html) alternatively executes the Fourier convolution on Nvidia hardware. The native code is called via *Java Native Access*. The source code as well as pre-compiled libraries for CUDA5 for Windows 64bit and Linux 64bit are provided online (http://fly.mpi-cbg.de/preibisch/nm/CUDA_code_conv3d.zip). Note that for Windows the DLL has to be placed in the Fiji directory, for Linux in a subdirectory called *lib/linux64* and that the current version of the Nvidia CUDA driver needs to be installed on the system.

14.5 BUILDING THE CUDA CODE

Using the native CUDA code is unfortunately not as easy as using Fiji. If the provided pre-compiled libraries do not work, first make sure you have the current Nvidia CUDA driver (<https://developer.nvidia.com/cuda-downloads>) installed and the samples provided by Nvidia work.

If Fiji still does not recognize the Nvidia CUDA capable devices, you might need to compile the CUDA source code (http://fly.mpi-cbg.de/preibisch/nm/CUDA_code_conv3d.zip). The supposedly simplest way is to use CMAKE, it is setup to compile directly. If, for some reason there are problems compiling it using CMAKE, you can try to compile it directly. Here is the command required to compile the CUDA library under linux, be sure to adapt the paths correctly.

```
nvcc convolution3Dfft.cu --compiler-options '-fPIC' -shared -lcudart -lcufft
-l/opt/cuda5/include/ -L/opt/cuda5/lib64 -lcuda -o libConvolution3D_fftCUDAlib.so
```

15. NUCLEI-BASED ALIGNMENT OF THE C. ELEGANS L1 LARVAE

In order to achieve a good deconvolution result, the individual views must be registered with very high precision. To achieve that, we match fluorescent beads that are embedded into the agarose with subpixel accuracy. However, in *C. elegans* during larval stages, the cuticle itself acts as a lense refracting the light sheet, which results in a slight misalignment of data inside the specimen. We therefore apply a secondary alignment step, which identifies corresponding nuclei in between views using geometric local descriptor matching,¹⁴ and from that estimates an affine transformation model for each view correcting for the refraction due to the cuticle. The algorithm works similar to the bead-based registration^{14,21} and is implemented in Fiji as a plugin called *Descriptor-based series registration* (Preibisch, unpublished software).

16. OTHER RELATED LITERATURE

The field of multi-view deconvolution is large and diverse; many areas of science contribute including medical science, astronomy, microscopy and the classical computer science. Within the focus of this publications it is not possible to discuss all aspects (e.g. multi-channel deconvolution). We therefore list other publications that contributed to various aspects of multi-image deconvolution.^{25,27–37}

REFERENCES

1. Huisken, J., Swoger, J., Bene, F. D., Wittbrodt, J., and Stelzer, E. H. K., "Optical sectioning deep inside live embryos by selective plane illumination microscopy," *Science* **305** (5686), 1007–1010 (2004).
2. Keller, P. J., Schmidt, A. D., Wittbrodt, J., and Stelzer, E. H. K., "Reconstruction of zebrafish early embryonic development by scanned light sheet microscopy," *Science* **322**(5904), 1065 (2008).
3. Truong, T. V., Supatto, W., Koos, D. S., Choi, J. M., and Fraser, S. E., "Deep and fast live imaging with two-photon scanned light-sheet microscopy," *Nat. Methods* **8**, 757–760 (Sep 2011).
4. Swoger, J., Verveer, P. J., Greger, K., Huisken, J., and Stelzer, E. H. K., "Multi-view image fusion improves resolution in three-dimensional microscopy," *Opt. Express* **15**(13), 8029–8042 (2007).
5. Shepp, L. and Vardi, Y., "Maximum likelihood reconstruction for emission tomography," *Medical Imaging, IEEE Transactions on* **1**(2), 113–122 (1982).
6. Hudson, H. and Larkin, R., "Accelerated image reconstruction using ordered subsets of projection data," *Medical Imaging, IEEE Transactions on* **13**(4), 601–609 (1994).
7. Verveer, P., Swoger, J., Pampaloni, F., Greger, K., Marcello, M., and Stelzer, E. H. K., "High-resolution three-dimensional imaging of large specimens with light sheet-based microscopy," *Nature Methods* **4**(4), 311–313 (2007).
8. Bonettini, S., Zanella, R., and Zanni, L., "A scaled gradient projection method for constrained image deblurring," *Inverse Problems* **25**(1), 015002 (2009).
9. Krzic, U., *Multiple-view microscopy with light-sheet based fluorescence microscope*, phd thesis, University of Heidelberg (2009).
10. Temerinac-Ott, M., Ronneberger, O., Ochs, P., Driever, W., Brox, T., and Burkhardt, H., "Multiview deblurring for 3-d images from light-sheet-based fluorescence microscopy," *Image Processing, IEEE Transactions on* **21**, 1863–1873 (april 2012).
11. Richardson, W. H., "Bayesian-based iterative method of image restoration," *Journal of the Optical Society of America* **62**, 55–59 (1972).
12. Lucy, L. B., "An iterative technique for the rectification of observed distributions," *Astronomical Journal* **79**(6), 745–754 (1974).
13. Dempster, A. P., Laird, N. M., and Rubin, D. B., "Maximum likelihood from incomplete data via the em algorithm," *JOURNAL OF THE ROYAL STATISTICAL SOCIETY, SERIES B* **39**(1), 1–38 (1977).
14. Preibisch, S., Saalfeld, S., Schindelin, J., and Tomancak, P., "Software for bead-based registration of selective plane illumination microscopy data," *Nature Methods* **7**, 418–419 (Jun 2010).

15. Long, F., Peng, H., Liu, X., Kim, S., and Myers, E., "A 3d digital atlas of *c. elegans* and its application to single-cell analyses," *Nature Methods* **6**, 667–672 (2009).
16. Keller, P. J., Schmidt, A. D., Santella, A., Khairy, K., Bao, Z., Wittbrodt, J., and Stelzer, E. H., "Fast, high-contrast imaging of animal development with scanned light sheet-based structured-illumination microscopy," *Nat. Methods* **7**, 637–642 (Aug 2010).
17. Pitrone, P. G., Schindelin, J., Stuyvenberg, L., Preibisch, S., Weber, M., Eliceiri, K. W., Huisken, J., and Tomancak, P., "Openspim: an open-access light-sheet microscopy platform," *Nature Methods* **7**, 598–599 (Jun 2013).
18. Schindelin, J., Arganda-Carreras, I., Frise, E., Kaynig, V., Longair, M., Pietzsch, T., Preibisch, S., Rueden, C., Saalfeld, S., Schmid, B., Tinevez, J. Y., White, D. J., Hartenstein, V., Eliceiri, K., Tomancak, P., and Cardona, A., "Fiji: an open-source platform for biological-image analysis," *Nat. Methods* **9**, 676–682 (Jul 2012).
19. Pietzsch, T., Preibisch, S., Tomancák, P., and Saalfeld, S., "ImgLib2 – generic image processing in Java," *Bioinformatics* **28**, 3009–3011 (Nov 2012).
20. Tikhonov, A. N. and Arsenin, V. Y., [*Solutions of Ill-posed problems*], W.H. Winston (1977).
21. Preibisch, S., *Reconstruction of Multi-Tile Microscopic Acquisitions*, phd thesis, Technical University Dresden (2011).
22. Kaufman, L., "Implementing and accelerating the em algorithm for positron emission tomography," *Medical Imaging, IEEE Transactions on* **6**(1), 37–51 (1987).
23. Merziger, G., Wirth, T., Wille, D., and Mühlbach, G., [*Formeln + Hilfen zur höheren Mathematik*], Binomi Verlag, 4th ed. (2004).
24. Singh, M. K., Tiwary, U. S., and Kim, Y.-H., "An adaptively accelerated lucy-richardson method for image deblurring," *EURASIP J. Adv. Signal Process* **2008** (2008).
25. Blume, M., Zikic, D., Wein, W., and Navab, N., "A new and general method for blind shift-variant deconvolution of biomedical images," in [*MICCAI '07*], 743–750, Springer (2007).
26. Uddin, M. S., Lee, H. K., Preibisch, S., and Tomancak, P., "Restoration of uneven illumination in light sheet microscopy images," *Microsc. Microanal.* **17**, 607–613 (Aug 2011).
27. Rajagopalan, A. and Chaudhuri, S., "A recursive algorithm for maximum likelihood-based identification of blur from multiple observations," *IEEE TIP* **7**, 1075 –1079 (jul 1998).
28. Giannakis, G. and Heath, R.W., J., "Blind identification of multichannel fir blurs and perfect image restoration," *IEEE TIP* **9**, 1877 –1896 (nov 2000).
29. Sroubek, F. and Flusser, J., "Multichannel blind iterative image restoration," *Image Processing, IEEE Transactions on* **12**, 1094 – 1106 (sept. 2003).
30. de Vieilleville, F., Weiss, P., Lobjois, V., and Kouame, D., "Alternating direction method of multipliers applied to 3d light sheet fluorescence microscopy image deblurring using gpu hardware," 4872 –4875 (30 2011-sept. 3 2011).
31. Heintzmann, R. and Cremer, C., "Axial tomographic confocal fluorescence microscopy," *Journal of microscopy* **206**(1), 7–23 (2002).
32. Shaw, P., Agard, D. A., Hiraoka, Y., and Sedat, J., "Tilted view reconstruction in optical microscopy. three-dimensional reconstruction of drosophila melanogaster embryo nuclei," *Biophysical Journal* **55**(1), 101–110 (1989).
33. Agard, D. A., "Optical sectioning microscopy: cellular architecture in three dimensions," *Annual review of Biophysics and Bioengineering* **13**(1), 191–219 (1984).
34. Agard, D. A., Hiraoka, Y., Shaw, P., and Sedat, J. W., "Fluorescence microscopy in three dimensions," *Methods in cell biology: Fluorescence microscopy of living cells in culture. Quantitative fluorescence microscopy-imaging and spectroscopy.* , 353–377 (1989).
35. Verveer, P. J. and Jovin, T. M., "Improved restoration from multiple images of a single object: application to fluorescence microscopy," *Applied Optics* **37**(26), 6240–6246 (1998).

36. Heintzmann, R., Kreth, G., and Cremer, C., "Reconstruction of axial tomographic high resolution data from confocal fluorescence microscopy: a method for improving 3d fish images," *Analytical Cellular Pathology* **20**(1), 7–15 (2000).
37. Holmes, T. J. and Liu, Y. H., "Acceleration of maximum-likelihood image restoration for fluorescence microscopy and other noncoherent imagery," *Journal of the Optical Society of America A* **8**(6), 893–907 (1991).